Approach to QCD phase diagram based on the imaginary chemical potential method

管野, 淳平

https://doi.org/10.15017/1931695

出版情報：九州大学, 2017, 博士（理学）, 課程博士
バージョン：
権利関係：

Approach to QCD phase diagram based on the imaginary chemical potential method

Junpei Sugano

Theoretical Nuclear Physics, Department of Physics
Graduate School of Science, Kyushu University
744, Motooka, Nishi-ku, Fukuoka 819-0395, Japan

Abstract

Matters in our world are composed of the quarks that interact with each other through the strong interaction mediated by gluons. The Quantum Chromodynamics (QCD) is the non-abelian gauge theory that describes the dynamics of quarks and gluons. One of remarkable properties of the QCD is asymptotic freedom, which makes coupling constant of the strong interaction decrease as increasing the energy scale and vice versa. In virtue of the asymptotic freedom, it is expected that the quark-gluon system takes various states, in response to the change of external parameters. It is challenging and interesting in hadron physics to clarify properties of the QCD under various external parameters, which leads to understanding of the early universe, neutron star physics and so on. In particular, toward understanding of the inner structure of neutron star, it is essential to study the QCD and its phase diagram under finite light-quark chemical potential μ_l, isospin chemical potential $\mu_{\rm iso}$, and strange-quark chemical potential $\mu_{\rm s}$.

Among the theoretical approaches, lattice QCD (LQCD) simulations are the most reliable framework, since it is the first-principle calculation of the QCD. LQCD simulation, however, suffers from the sign problem and thereby the simulation is difficult to work. It is thus important to gather solid information from the regions where the sign problem does not occur.

In this thesis, we focus on the following three imaginary chemical potential regions; (A) the imaginary μ_l region, (B) the imaginary μ_l and $\mu_{\rm s}$ region, (C) the imaginary μ_l and $\mu_{\rm iso}$ region. In these regions, LQCD simulations can be performed since there is no sign problem. Information on real μ_l, $\mu_{\rm iso}$, $\mu_{\rm s}$ regions is extracted by the analytic continuation from the imaginary region to the real one. We call this procedure "imaginary chemical potential method". It is thus important to know the analyticity of the QCD in order to apply the imaginary chemical potential method.

For region (A), the phase structure of the QCD has been investigated in detail, and it was found that the first-order Roberge-Weiss phase transition prevents the analytic continuation. Due to this, information on the real-μ_l dependence of physical quantities is limited up to $\mu_l/T \lesssim 1$, where T is temperature. To analyze the region $\mu_l/T \gtrsim 1$, it is convenient to use the effective models that are consistent with LQCD data in $\mu_l/T \lesssim 1$. Our purpose in region (A) is to construct a reliable effective model to describe the quark degree of freedom. We aim at determining the strength of the

vector-type four-quark interaction in an effective model, since the interaction largely affects on neutron-star masses and the QCD phase structure. For this purpose, we use LQCD data on the light-quark number density derived with the imaginary chemical potential method. Based on the constructed model, we analyze the QCD phase diagram and the inner core of neutron star.

As for region (B) and (C), there are little studies and it is therefore desirable to explore properties of the QCD there. In region (B), we take two approaches; one is a theoretical approach based on the QCD and the other is a model approach with the same properties as the QCD as possible. The latter is a qualitative approach, but it allows us flexible investigation. In region (A), the analyticity is lost by the presence of the first-order phase transition. We thus study the location of the first-order transition in region (B). Furthermore, we search the condition imposed on imaginary μ_l and $\mu_{\rm s}$, in order to obtain the region where no first-order transition takes place. If such a region exists, it is useful for the imaginary chemical potential method.

In the real $\mu_{\rm iso}$ region, the QCD has a characteristic phase, called the charged-pion condensate phase. In the phase, flavor $\mathrm{U_{I_3}}(1)$ symmetry of the QCD is spontaneously broken and the sign problem is expected to be severe. This means that LQCD simulations become unfeasible there. Meanwhile, it is predicted that the charged-pion condensate does not occur in the imaginary $\mu_{\rm iso}$, at least for $\mu_l = 0$. We show that this prediction is true also for non-zero μ_l, i.e., in region (C). For the proof, we use QCD inequalities. This approach enables us to see which symmetry is spontaneously broken or not, based on the QCD. The proof is done by demonstrating that $\mathrm{U_{I_3}}(1)$ symmetry is not spontaneously broken in region (C).

This thesis is based on the following three papers:

- Determination of hadron-quark phase transition line from lattice QCD and two-solar-mass neutron star observations,
  J. Sugano, H. Kouno, and M. Yahiro, Phys. Rev. D **94**, 014024 (2016).

- Properties of 2+1-flavor QCD in the imaginary chemical potential region: A model approach,
  J. Sugano, H. Kouno, and M. Yahiro, Phys. Rev. D **96**, 014028 (2017).

- QCD-inequality analyses on pion condensate at real and imaginary isospin chemical potentials under finite imaginary quark chemical potential,
  J.Sugano, H. Kouno, and M. Yahiro, arXiv:1711.00663 (to be published in Physical Review D).

Acknowledgements

First of all, I would like to express my sincere gratitude to my supervisor Prof. Masanobu Yahiro. The discussions with him were exciting for me and I learned many knowledge on hadron physics, particle physics, and astrophysics. He also showed me attitude as researcher and educator. In addition, he always supported and encouraged me on my research since I was undergraduate student. Thanks to him, I accomplished my Dr. thesis.

I would like to express appreciation to Prof. Hiroaki Kouno. He gave me many comments and insights on hadron physics. His comments allowed me to grasp the essence and intuitive understanding of hadron physics. He also taught me rigor of research.

I would like to express my appreciation to Associate Prof. Yoshifumi R. Shimizu and Assistant Prof. Takuma Matsumoto. Through their seminar, I could learn how nuclear structure and reaction, and quantum field theory are interest and difficult. Moreover, they gave me many comments in the view point of nuclear physicist.

I was supported by many seniors and juniors of theoretical nuclear physics laboratory and would like to express my gratitude to them. I especially would like to thank to six seniors. First, I would like to appreciate to two seniors, Dr. Kouji Kashiwa and Dr. Junichi Takahashi. They gave me warm words and valuable comments on research. Next, I would like to express my appreciation to four seniors, Dr. Shin Watanabe, Dr. Masahiro Ishii, Dr. Satoru Sasabe, and Dr. Masakazu Toyokawa. They were always open and taught me many knowledges on hadron physics, nuclear physics, and computational technique in casual conversation. Furthermore, I did enjoy private life with them.

I would like to extend my appreciation to people of other laboratories. In particular, I would like to express my special thanks to Aya Kasai. She taught me many ideas on particle physics and I was always encouraged by her warm words.

I would like to show my appreciation to Yuki Yamaji, Hiromi Tsuchijima, Megumi Ieda, Noriko Taguchi, Mayumi Takaki, and Mariko Komori for practical supports to me and amusing conversation.

This work was supported by Grants-in-Aid for Scientific Research (No. 27-7804) from the Japan Society for the Promotion of Science (JSPS).

Finally, I would like to express my deepest appreciation to my family: my parents and sisters. They always encouraged me through all my life.

Contents

List of Figures

List of Tables

Chapter 1

Introduction

1.1 QCD in Minkowski space-time

The QCD in Minkowski space-time is constructed so that its Lagrangian is invariant under local gauge transformation, belonging to color SU($N_{\rm c}$) group, where $N_{\rm c}$ is the number of color. From any function $U(x) \in {\rm SU}(N_{\rm c})$, color SU($N_{\rm c}$) gauge transformation is defined by

$$\begin{aligned} q(x) &\rightarrow U(x)q(x), \\ A_\mu(x) &\rightarrow U(x)A_\mu(x)(U(x))^{-1} + i(\partial_\mu U(x))(U(x))^{-1}, \end{aligned} \tag{1.1}$$

where $q = (q_1, \cdots, q_{N_{\rm f}})$ is the quark field with $N_{\rm f}$ flavors and A_μ is the gluon field. The function $U(x)$ is written as $U(x) = \exp(i\theta^a(x)T^a)$ with any real function $\theta^a(x)$, the generators T^a, and color indices $a = 1, \cdots, N_{\rm c}^2 - 1$. In the gluon field, the notation $A_\mu = gA_\mu^a T^a$ is used, i.e., the field A_μ includes the gauge coupling g in itself. Hereafter, we set $N_{\rm c} = 3$. In this case, $T^a = \lambda^a/2$ with the Gell-Mann matrices λ^a.

Imposing the invariance under Eq. (1.1), the QCD Lagrangian is given by [1)]

$$\mathcal{L}_{\rm QCD} = \bar{q}(i\gamma^\mu D_\mu - \hat{m})q - \frac{1}{2g^2}{\rm Tr}_{\rm c}F^{\mu\nu}F_{\mu\nu}. \tag{1.2}$$

In Eq. (1.2), $D_\mu = \partial_\mu + iA_\mu$ is the covariant derivative and $\hat{m} = {\rm diag}(m_1, \cdots, m_{N_{\rm f}})$ is the current quark-mass matrix in flavor space. The field strength of the gluon field is defined by

$$F_{\mu\nu} = \frac{1}{i}\left[D_\mu, D_\nu\right] = \partial_\mu A_\nu - \partial_\nu A_\mu + i\left[A_\mu, A_\nu\right]. \tag{1.3}$$

The symbol ${\rm Tr}_{\rm c}$ in the right side of Eq. (1.2) denotes the trace in color space.

In experiments, six quarks have been confirmed so far, i.e., up (u), down (d), strange (s), charm (c), beauty (b), and top (t). The values of the current masses are tabulated in Table 1.1. The masses of c-, b-, and t-quarks are

[1)] We do not consider the so-called θ term that violates *CP* symmetry [1, 2, 3].

Table 1.1: Summary of the current quark mass [4].

m_{u} [MeV]	m_{d} [MeV]	m_{s} [MeV]	m_{c} [GeV]	m_{b} [GeV]	m_{t} [GeV]
2.2	4.7	96	1.27	4.18	160

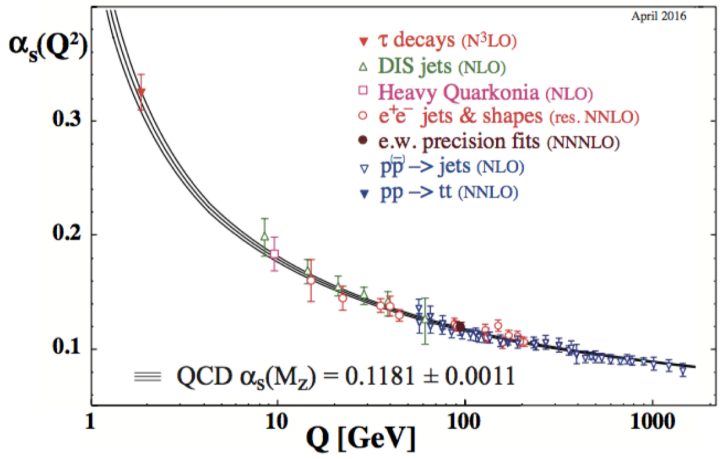

Figure 1.1: The energy scale Q dependence of the coupling constant $\alpha_s(Q^2)$ of strong interaction. The experimental data are presented with the error bars, and band means the theoretical prediction from the QCD. Figure is taken from [4].

much heavier than those of u-, d-, and s-quarks. In this thesis, we concentrate on the energy scale in which contributions of the heavy quarks can be ignored, and take into account only u-, d-, and s-quarks. Among these three quarks, u- and d-quarks have almost the same masses as each other, and hence we can set $m_{\mathrm{u}} = m_{\mathrm{d}} = m_l$ as a good approximation. Under this approximation, we call the QCD with u- and d-quarks "2-flavor QCD". Meanwhile, s-quark has a relatively large mass compared with u- and d-quarks, and consequently, the approximation $m_{\mathrm{s}} = m_l$ may not work well. Whenever we consider the QCD with the conditions of $m_{\mathrm{u}} = m_{\mathrm{d}} = m_l$ and $m_{\mathrm{s}} > m_l$, we call it "2+1-flavor QCD".

One of the most important properties of the QCD is the asymptotic freedom. Due to this property, the strength $\alpha_{\mathrm{s}}(Q^2)$ of the quark-quark interaction decreases as increasing the energy scale Q. The Q dependence can be calculated from the renormalization group equation. Up to the one-loop order, the result is given by [5, 6]

$$\alpha_{\mathrm{s}}(Q^2) = \frac{g^2(Q^2)}{4\pi^2} = \frac{12\pi}{(33 - 2N_{\mathrm{f}})\log(Q^2/\Lambda^2_{\mathrm{QCD}})}. \tag{1.4}$$

In Eq. (1.4), $\Lambda_{\mathrm{QCD}} \sim 200$ MeV is the characteristic energy scale of the QCD. The validity of Eq. (1.4) has already been confirmed from the comparison

with various experimental data, measured such as in the deep inelastic scattering between lepton; see Fig. 1.1.

1.2 QCD phase diagram

It can be seen in Fig. 1.1 that the strength $\alpha_{\rm s}(Q^2)$ becomes quite large as decreasing Q. This means that the non-perturbative nature comes out as decreasing temperature T and quark chemical potential $\mu_{\rm q}$. Here, $\mu_{\rm q}$ is given by the average of the chemical potential for each quark, [2)]

$$\mu_{\rm q} = \frac{1}{N_{\rm f}} \sum_{i=1}^{N_{\rm f}} \mu_i, \tag{1.5}$$

where $N_{\rm f} = 2$ for the 2-flavor QCD and $N_{\rm f} = 3$ for the 2+1-flavor one.

The non-perturbativeness causes two characteristic phenomena; one is the confinement of quark and the other is the spontaneous chiral symmetry breaking. Meanwhile, the asymptotic freedom predicts that the deconfinement of quarks and the chiral symmetry restoration takes place at some T and $\mu_{\rm q}$, which are regarded as phase transitions. This prediction leads to the QCD phase diagram.

From this section, temperature and quark chemical potential are taken into account. The Euclidean space-time formalism is then used. Based on the Euclidean QCD, we explain the confinement of quarks and the spontaneous chiral symmetry breaking, introducing $\mathbb{Z}_3$ symmetry and chiral symmetry that are closely related to these phenomena. We also present the fundamental structure of the QCD phase diagram and summarize the current status of the diagram.

1.2.1 QCD in Euclidean space-time

The Euclidean space-time formalism enables us to treat the QCD at finite T and $\mu_{\rm q}$. The starting point is to introduce a Euclidean time τ by the replacement $x_4^{\rm E} = \tau = ix^0$ [7]. Then, the QCD Lagrangian in Euclidean space-time is given by

$$\mathcal{L}_{\rm QCD}^{\rm E} = \bar{q}^{\rm E}(\gamma_\mu^{\rm E} D_\mu^{\rm E} + \hat{m}) q^{\rm E} + \frac{1}{2g^2} {\rm Tr}_{\rm c} F_{\mu\nu}^{\rm E} F_{\mu\nu}^{\rm E}. \tag{1.6}$$

As for the detail of notations, see Appendix. A.

In the Euclidean formalism, the τ-direction is compactified and limited into the region $[0, \beta]$, where $\beta = 1/T$. Then, the fields $q^{\rm E}(\tau, \boldsymbol{x})$ and $A_\mu^{\rm E}(\tau, \boldsymbol{x})$ should satisfy the boundary conditions,

$$q^{\rm E}(\tau + \beta, \boldsymbol{x}) = -q^{\rm E}(\tau, \boldsymbol{x}), \tag{1.7}$$

$$A_\mu^{\rm E}(\tau + \beta, \boldsymbol{x}) = A_\mu^{\rm E}(\tau, \boldsymbol{x}), \tag{1.8}$$

[2)] If we regard u- and d-quarks as degenerate particles, $\mu_{\rm u} = \mu_{\rm d}$ should be imposed.

respectively. The anti-periodic boundary condition is imposed on the quark field, while the gluon field satisfies the periodic boundary condition. This difference comes from statistics, i.e., the quark field obeys the Fermi-Dirac statistics and the gluon field does the Bose-Einstein statistics. Hereafter, we use the Euclidean representation and drop the superscript "E".

1.2.2 Confinement and deconfinement of quark

In our world, the quarks form hadrons by strong interaction and are not observed alone. Therefore, the fundamental degree of freedom at the low-energy regime is not quark but hadron, such as nucleon and pion. This phenomenon is called the confinement of quark. It is possible, however, that quark can be free from the confinement in the high T and/or $\mu_{\rm q}$ region, because the interaction between quarks is weaken. Then, the transition from the confinement state to the deconfinement one takes place at some value of T and $\mu_{\rm q}$, and the fundamental degree of freedom is switched from hadron to quark. In the following, we introduce the Polyakov loop that is an indicator to distinguish the confinement and deconfinement states at finite T and $\mu_{\rm q}$.

Now, we consider the gauge transformation (1.1) generated by $U(\tau, \boldsymbol{x})$ with the twisted-boundary condition,

$$U(\tau + \beta, \boldsymbol{x}) = z_k U(\tau, \boldsymbol{x}), \tag{1.9}$$

where z_k is defined by

$$z_k = \exp\left[\frac{2\pi i k}{3}\right] \tag{1.10}$$

with $k = -1, 0, 1$. Indeed, we can construct $U(\tau, \boldsymbol{x})$ satisfying the condition (1.9) as

$$U(\tau, \boldsymbol{x}) = (z_k)^{\frac{\tau}{\beta}} \mathbf{1}_{\rm c} = \exp\left[\frac{2\pi i k}{3}\frac{\tau}{\beta}\right] \mathbf{1}_{\rm c}. \tag{1.11}$$

Here, the unit matrix in color space is expressed by $\mathbf{1}_{\rm c}$. The factors z_k belongs to the $\mathbb{Z}_3$ group which is a center of color SU(3) group. The gauge transformation by Eq. (1.11) is thus called $\mathbb{Z}_3$ transformation.

Let us perform the $\mathbb{Z}_3$ transformation for the QCD Lagrangian (1.6). The $\mathbb{Z}_3$ transformation is a kind of gauge transformations and hence makes the QCD Lagrangian invariant. From the gauge-transformation law of A_μ shown in Eq. (1.1), the boundary condition (1.8) is also unchanged. Therefore, the QCD without dynamical quark, such as in the pure gauge limit, is exactly symmetric under $\mathbb{Z}_3$ transformation. This symmetry is called $\mathbb{Z}_3$ symmetry.

Now, we define the Polyakov-loop operator by

$$L(\boldsymbol{x}) = \frac{1}{3}\mathcal{P}\exp\left[i\int_0^\beta d\tau\ A_4(\tau, \boldsymbol{x})\right], \tag{1.12}$$

where $\mathcal{P}$ denotes the path ordering. The $\mathbb{Z}_3$ transformation changes the gluon field A_4 into

$$A_4(\tau, \boldsymbol{x}) \ \rightarrow \ A_4(\tau, \boldsymbol{x}) + \frac{2\pi k}{3}\frac{1}{\beta}\mathbf{1}_{\mathrm{c}} \tag{1.13}$$

and therefore

$$L(\boldsymbol{x}) \ \rightarrow \ z_k L(\boldsymbol{x}) \tag{1.14}$$

is deduced. Furthermore, the free energy F_q of the single heavy quark can be written by

$$\mathrm{e}^{-\beta F_q} = \langle \Phi(\boldsymbol{x}) \rangle \,, \tag{1.15}$$

where $\Phi(\boldsymbol{x})$ is the Polyakov loop $\Phi(\boldsymbol{x}) = \mathrm{Tr}_{\mathrm{c}} L(\boldsymbol{x})$ and $\langle \cdots \rangle$ denotes the expectation value [8]. The $\mathbb{Z}_3$ transformation changes $\Phi(\boldsymbol{x})$ as

$$\Phi(\boldsymbol{x}) \ \rightarrow \ z_k \Phi(\boldsymbol{x}), \tag{1.16}$$

which is the same as in $L(\boldsymbol{x})$. From this fact, its expectation value suggests

$\langle \Phi \rangle = 0 \quad \rightarrow \quad \mathbb{Z}_3$ symmetry is preserved and $F_q = \infty, \ \therefore$ confinement
$\langle \Phi \rangle \neq 0 \quad \rightarrow \quad \mathbb{Z}_3$ symmetry is broken and F_q is finite value, $\ \therefore$ deconfinement

It is thus concluded that $\langle \Phi \rangle$ is available for the order parameter of $\mathbb{Z}_3$ symmetry, and we can distinguish the confinement and deconfinement phases by the value of $\langle \Phi \rangle$.

Meanwhile, it is found from the transformation law $q \rightarrow Uq$ that the quark field satisfies the new boundary condition

$$q(\tau + \beta, \boldsymbol{x}) = -z_k q(\tau, \beta), \tag{1.17}$$

instead of Eq. (1.7). This means that $\mathbb{Z}_3$ symmetry of the QCD is explicitly broken through the boundary condition of quark field, although the Lagrangian itself is symmetric. Therefore, the discussion mentioned above does not hold for the system with the dynamical quark, and the Polyakov loop is thus not an exact order parameter in the situation. However, $\langle \Phi \rangle$ is commonly used for the order parameter of $\mathbb{Z}_3$ symmetry, even if we take into account the dynamical quark. In this thesis, we judge the confinement and deconfinement phases through $\langle \Phi \rangle$, and simply denote $\langle \Phi \rangle$ as Φ.

1.2.3 Spontaneous chiral symmetry breaking

Due to the confinement mechanism, quarks form hadrons, such as nucleon, in the low-T and -μ_{q} region. Proton is composed of two u-quarks and one d-quark. The mass of proton is about 15 MeV under naive consideration, but the actual value is about 940 MeV. As for the mesonic sector, the mass of

pion ~ 140 MeV is much lighter than the other mesons, e.g., ρ-meson mass ~ 770 MeV, although ρ-meson has the same quark-composition as pion. The spontaneous chiral symmetry breaking is a key to understanding these mass gaps.

We begin with the 2-flavor QCD Lagrangian,

$$\mathcal{L}_{\rm QCD} = \bar{q}(\gamma_\mu D_\mu + m_l)q + \frac{1}{2g^2}{\rm Tr_c} F_{\mu\nu}F_{\mu\nu}. \tag{1.18}$$

The mass matrix is proportional to the unit matrix of flavor space and hence we simply denote the mass term as $m_l\bar{q}q$. We first take the case of $m_l = 0$, i.e., the chiral limit. In the chiral limit, it is convenient to introduce two-component right- and left-handed spinor fields, $q_{\rm R,L}$. With the projection operators $P_{\rm R,L} = (1 \pm \gamma_5)/2$ for $\gamma_5 = \gamma_1\gamma_2\gamma_3\gamma_4$, the field q is decomposed into

$$q = P_{\rm R}q + P_{\rm L}q = q_{\rm R} + q_{\rm L}. \tag{1.19}$$

The expression (1.18) with $m_l = 0$ thus becomes

$$\mathcal{L}_{\rm QCD} = \bar{q}_{\rm R}\gamma_\mu D_\mu q_{\rm R} + \bar{q}_{\rm L}\gamma_\mu D_\mu q_{\rm L} + \frac{1}{2g^2}{\rm Tr_c} F_{\mu\nu}F_{\mu\nu}, \tag{1.20}$$

where Dirac conjugates $\bar{q}_{\rm R,L}$ are defined by

$$\bar{q}_{\rm R} = \bar{q}P_{\rm L}, \quad \bar{q}_{\rm L} = \bar{q}P_{\rm R}. \tag{1.21}$$

The kinetic term of quark field in Eq. (1.20) is separated into the right-handed and the left-handed parts of q. Hence, Eq. (1.20) is invariant under the global ${\rm U(2)_R} \otimes {\rm U(2)_L}$ transformation defined by

$$q_{\rm R} \ \to \ {\rm e}^{i\theta^a_{\rm R}\tau^a} q_{\rm R}, \quad q_{\rm L} \ \to \ {\rm e}^{i\theta^a_{\rm L}\tau^a} q_{\rm L} \tag{1.22}$$

with the independent transformation parameters $\theta^a_{\rm R,L}$ and flavor indices $a = 0, \cdots, 3$. Here, τ^0 is the 2×2 unit matrix in flavor space and the Pauli matrices are given by $\vec{\tau}$. ${\rm U(2)_R}\otimes{\rm U(2)_L}$ symmetry is rewritten into ${\rm U(1)_V}\otimes{\rm U(1)_A}\otimes {\rm SU(2)_V}\otimes{\rm SU(2)_A}$ and hence we obtain four subgroups; see Appendix B. In these subgroups, ${\rm U(1)_A}$ symmetry is explicitly broken by a quantum anomaly [9, 10]. The 2-flavor QCD Lagrangian thus has ${\rm U(1)_V}\otimes{\rm SU(2)_V}\otimes{\rm SU(2)_A}$ symmetry in the chiral limit at the Lagrangian level.

If the current mass m_l is finite, the mass term breaks chiral symmetry explicitly. To see this, let us rewrite the mass term $m_l\bar{q}q$ as

$$m_l\bar{q}q = m_l(\bar{q}_{\rm L}q_{\rm R} + \bar{q}_{\rm R}q_{\rm L}). \tag{1.23}$$

This expression shows that the mass term mixes the right- and left-handed components of quark and hence chiral symmetry is explicitly broken. In the case that the Lagrangian includes only the light quarks, however, chiral symmetry is still good approximation, because the value of m_l is much smaller

than a typical energy scale of the QCD; $m_l/\Lambda_{\rm QCD} \sim O(10^{-3})$. Therefore, the 2-flavor QCD Lagrangian (1.18) approximately possesses chiral symmetry.

In Ref. [11], Nambu and Jona-Lasinio showed that if the quark-quark interaction is sufficiently strong, chiral symmetry is broken by the appearance of a non-trivial vacuum, even though the symmetry is preserved at the Lagrangian level. Then, only $\mathrm{U(1)_V}\otimes\mathrm{SU(2)_V}$ symmetry is left in the low-energy region [3]. In the realized vacuum, the quantity $\sigma_f = \langle\bar{q}_f q_f\rangle$, called chiral condensate, does not vanish and yields an additional mass to the quark. This is referred to as the spontaneous chiral symmetry breaking. The acquirement of mass through σ_f explains why nucleon mass is much heavier than the naively estimated value ~ 15 MeV.

Furthermore, they demonstrated that massless particle is accompanied with the spontaneous chiral symmetry breaking. Since Goldstone reached the same result [13], massless particle is called Nambu-Goldstone (NG) boson. Pion is just a NG boson and hence its mass is very light. In this way, the spontaneous chiral symmetry breaking well explains the mass spectrum of hadron. The asymptotic freedom predicts that the quark-quark interaction becomes very strong in the low-energy region, and it is believed that the chiral symmetry breaking takes place there [4].

On the contrary, it is expected from the asymptotic freedom that chiral symmetry is recovered in the high-T and/or -$\mu_{\rm q}$ region. To see whether the chiral symmetry breaking or not, it is useful to take the chiral condensate σ_f as an order parameter of the chiral symmetry breaking. Then, we can characterize the phase of system at finite T and $\mu_{\rm q}$ as

$$\begin{aligned} \sigma_f \neq 0 \quad &\rightarrow \quad \text{chiral symmetry broken phase} , \\ \sigma_f = 0 \quad &\rightarrow \quad \text{chiral symmetry restored phase} , \end{aligned}$$

respectively. If we replace the group $\mathrm{U(2)_R}\otimes\mathrm{U(2)_L}$ with $\mathrm{U(3)_R}\otimes\mathrm{U(3)_L}$, the same discussion is applicable to the 2+1-flavor case.

1.2.4 Structure of QCD phase diagram

From the order parameters σ_f and Φ, we can classify phases of the QCD and draw the QCD phase diagram in T-$\mu_{\rm q}$ plane in which hadron and quark-gluon states are represented. A sketch of the QCD phase diagram is presented in Fig. 1.2; See also Refs. [15, 16, 17, 18] for further details of the QCD phase diagram.

In the figure, there are two representative phases [5]. One is the hadron phase that is realized in the low T and the low $\mu_{\rm q}$ region. In this phase, quarks

[3] It was proved in Ref. [12] that vector-type symmetry, such as $\mathrm{U(1)_V}$ and $\mathrm{SU(2)_V}$, is not spontaneously broken in the QCD (Vafa-Witten theorem).

[4] In Ref. [14], it was numerically confirmed that σ_f is indeed finite.

[5] Throughout this thesis, we do not consider color superconductor phase, where quarks form cooper pair in color space. For the review, see Ref. [19] and references therein.

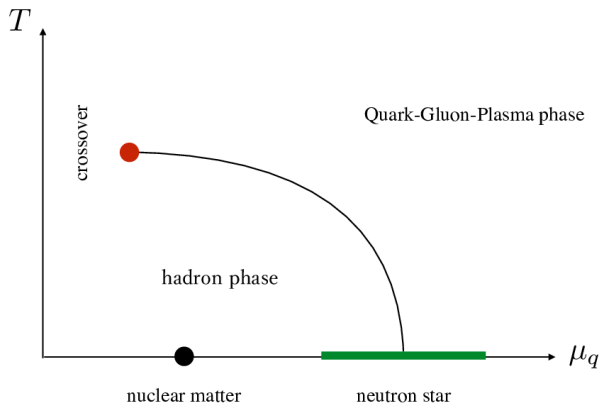

Figure 1.2: The QCD phase diagram in T-$\mu_{\rm q}$ plane.

and gluons are confined into hadron and the spontaneous chiral symmetry breaking also takes place; $\sigma_f \neq 0$ and $\Phi = 0$. Another phase is called Quark-Gluon Plasma (QGP) phase, or simply quark phase, that appears at large T and/or $\mu_{\rm q}$. The feature of this phase is that quarks and gluons are free from the confinement ($\Phi = 0$) and behave as free particles. In addition, chiral symmetry is restored in this phase ($\sigma_f \sim 0$).

The change from the hadron phase to the QGP phase can be regarded as a phase transition and occurs at some critical T and $\mu_{\rm q}$. Then, two-types of boundary exist, one being the chiral transition line and the other the deconfinement transition line. In particular, the latter is also referred to as a hadron-quark phase transition line, firstly predicted by Cabibbo and Parisi in Ref. [20] based on Hagedorn theory [21]. At $\mu_{\rm q}/T = 0$, the hadron-quark phase transition is crossover and takes place at $T_{\rm c} \sim 171$ MeV for the 2-flavor system [22], at $T_{\rm c} \sim 160$ MeV for the 2+1-flavor system [23, 24], respectively. On the other hand, the transition may be first-order for moderate $\mu_{\rm q}$, predicted by Asakawa and Yazaki [25]. If this scenario is true, there should be a critical end point (CEP) somewhere in the diagram. The search of a CEP is extensively done [15].

Recently, theoretical investigations of the QCD phase diagram have been made, particularly at $\mu_{\rm q}/T = 0$, because of progress of lattice QCD simulations explained in Sec. 1.3. In addition to the property of the hadron-quark transition, the behavior of the equation of state (EoS) is also mostly determined [26]. Along these lines, thermal properties of hadron and quark matters are steadily clarified at $\mu_{\rm q}/T = 0$.

As for $\mu_{\rm q}/T = \infty$, the EoS for cold and dense matter is essential tool of understanding properties of neutron star physics. In the nucleonic regime, robust studies on EoS of the symmetric and asymmetric nuclear matter were made, and various properties were understood, such as a role of many-body nuclear force [27, 28, 29]. In addition to the nuclear matter, possibility of the

hyperonic matter [29, 30] and the quark matter [31] may exist in the inner core of neutron star. This means that not only light-quark chemical potential $\mu_l = (\mu_{\rm u} + \mu_{\rm d})/2$ but also isospin chemical potential $\mu_{\rm iso} = (\mu_{\rm u} - \mu_{\rm d})/2$ and strange-quark chemical potential $\mu_{\rm s}$ become finite. In particular, due to the observations of two-solar-mass neutron star in Refs. [32, 33], whether the quark matter exists in the inner core of neutron star or not is extensively discussed. To answer this, it is important to know the phase structure and the interaction between quarks in the finite $(\mu_l, \mu_{\rm iso}, \mu_{\rm s})$ region.

In the theoretical approach, lattice QCD simulations are the most powerful tool of extracting information on the quark matter, but the simulations are difficult due to the sign problem. One of solutions to this difficulty is to consider the regions where the sign problem does not occur and information on finite $(\mu_l, \mu_{\rm iso}, \mu_{\rm s})$ are included. From the next section, we discuss lattice QCD simulations with finite $(\mu_l, \mu_{\rm iso}, \mu_{\rm s})$.

1.3 Lattice QCD

LQCD simulations are the first-principle calculation of the QCD formulated by Wilson [35]. It enables us to treat non-perturbative nature of the QCD. This is the strong points of LQCD simulations and we can obtain solid information on thermal properties of quark matter. In the simulations, the integrand of the QCD grand-canonical partition function $Z_{\rm QCD}$ determines whether the simulations can be performed or not. After introducing the expression of $Z_{\rm QCD}$ to be evaluated, we briefly review framework of LQCD simulations.

1.3.1 QCD grand-canonical partition function

By using the imaginary-time formalism [7] and Eq. (1.6), we can define the QCD grand-canonical partition function as

$$Z_{\rm QCD} = \int \mathcal{D}A\mathcal{D}\bar{q}\mathcal{D}q \ \exp\left[-\int_0^\beta d\tau \int d^3\boldsymbol{x}\,(\mathcal{L}_{\rm QCD} - \bar{q}\hat{\mu}\gamma_4 q)\right], \tag{1.24}$$

where $\hat{\mu} = {\rm diag}(\mu_{\rm u}, \mu_{\rm d}, \mu_{\rm s})$ in flavor space and the functional integral $\mathcal{D}A$ means

$$\mathcal{D}A = \prod_{\mu=1}^{4} \mathcal{D}A_\mu. \tag{1.25}$$

The quark field is included in Eq. (1.24) as a bilinear form, and hence we can perform the gauss integral for a Grassmann variable. The integral yields

$$Z_{\rm QCD} = \int \mathcal{D}A \ {\rm det}\mathcal{M}(\hat{\mu}){\rm e}^{-S_{\rm G}}, \tag{1.26}$$

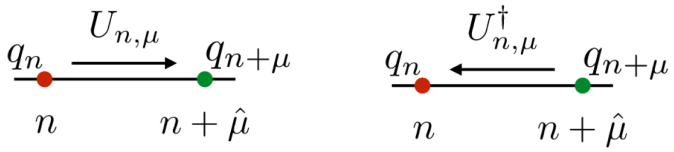

Figure 1.3: Sketch of the link variable. The variable $U_{n,\mu}$ goes from lattice point n to $n+\hat{\mu}$, while $U^\dagger_{n,\mu}$ does the inverse direction. The quark field on the point n and $n+\hat{\mu}$ is denoted by q_n and $q_{n+\mu}$.

where $S_{\rm G}$ is the pure gauge action and $\mathcal{M}(\hat{\mu})$ is the fermion matrix

$$\mathcal{M}(\hat{\mu}) = \mathcal{M}(\mu_{\rm u}, \mu_{\rm d}, \mu_{\rm s}) = \gamma_\mu D_\mu + \hat{m} - \hat{\mu}\gamma_4, \tag{1.27}$$

and its determinant is called the fermion determinant.

The QCD thermodynamic potential $\Omega_{\rm QCD}$ (per unit volume) is obtained from

$$\Omega_{\rm QCD} = -\frac{1}{\beta}\log Z_{\rm QCD}. \tag{1.28}$$

Other thermodynamic quantities can be derived from $\Omega_{\rm QCD}$. Also for the expectation value of any physical quantity $\mathcal{O}$, we can take the path-integral representation [7] as

$$\langle\mathcal{O}\rangle = \frac{1}{Z_{\rm QCD}}\int \mathcal{D}A\ \mathcal{O}{\rm det}\mathcal{M}(\hat{\mu}){\rm e}^{-S_{\rm G}}. \tag{1.29}$$

1.3.2 Sign problem

In LQCD, the QCD is discretized and formulated on a four-dimensional lattice with lattice spacing a. The quark field is putted on each lattice site and the gluon field is expressed by a link variable

$$U_{n,\mu} \equiv U(n, n+\hat{\mu}a) = \exp\left[iaA_\mu(n+\hat{\mu}/2)\right], \tag{1.30}$$

where n is the lattice point and $\hat{\mu}$ is the unit vector of μ-direction. The link variable describes the gluon propagating from x to $x+\hat{\mu}$. The Hermite conjugate of Eq. (1.30) is written by

$$U^\dagger_{n,\mu} = U_{n+\mu,-\mu} \tag{1.31}$$

and means the gluon propagating the inverse direction of $U_{n,\mu}$. The gluon field is thus treated so that it connects the neighborhood site; see Fig. 1.3.

By using the link variables, the grand-canonical partition function on the lattice is given by

$$Z_{\rm QCD} = \int \mathcal{D}U\ {\rm det}\mathcal{M}(\hat{\mu}){\rm e}^{-S_{\rm G}}, \tag{1.32}$$

i.e., $Z_{\rm QCD}$ is the sum of link variables. In LQCD simulations, the integrand $P(U) \equiv \det\mathcal{M}(\hat{\mu})\mathrm{e}^{-S_{\rm G}}$ is interpreted as a probability function. With this function, the link variable U is generated with the importance-sampling method of Monte-Carlo technique. Hence, we can directly generate the configuration of U from the QCD without any approximation.

The probability function $P(U)$ should have positivity in applying the Monte-Carlo technique and it depends on whether the fermion determinant has positivity. For $\mu_{\rm q} = (\mu_{\rm u} + \mu_{\rm d} + \mu_{\rm s})/3 = 0$, the fermion matrix satisfies γ_5-hermiticity:

$$\gamma_5\mathcal{M}(0)\gamma_5 = (\mathcal{M}(0))^\dagger. \tag{1.33}$$

Positivity of the fermion determinant $\det\mathcal{M}(0)$ is thus ensured and the Monte-Carlo method is available. However, the fermion determinant can be complex when $\mu_{\rm q} \neq 0$, since the relation

$$(\mathcal{M}(\hat{\mu}))^\dagger = \gamma_5\mathcal{M}(-\hat{\mu}^*)\gamma_5, \tag{1.34}$$

or equivalently,

$$(\mathcal{M}(\mu_{\rm u}, \mu_{\rm d}, \mu_{\rm s}))^\dagger = \gamma_5\mathcal{M}(-\mu_u^*, -\mu_d^*, -\mu_s^*)\gamma_5 \tag{1.35}$$

does not guarantee positivity of the fermion determinant. Hence, it is difficult to access to the finite $\mu_{\rm q}$ region with LQCD. This is the well-known sign problem [34] and the shortcoming of LQCD.

Some methods of circumventing the sign problem were proposed so far, e.g., the imaginary chemical potential method, the reweighting method, the Taylor expansion method, and so on. Among these methods, we pick up the imaginary chemical potential method.

1.4 Imaginary chemical potential method

In this section, we discuss the imaginary chemical potential method [36, 37]. In particular, we focus on the three regions; (A) imaginary μ_l region, (B) imaginary μ_l and $\mu_{\rm s}$ region, (C) imaginary μ_l and $\mu_{\rm iso}$ region. For each region, our main purpose is also presented.

1.4.1 Region (A): 2-flavor case

We first take $\mu_{\rm u} = \mu_{\rm d} = \mu_l$ and $\mu_{\rm s} = 0$. The imaginary chemical potential is introduced by the replacement $\mu_l \to i\theta_l T$, where θ_l is a dimensionless light-quark chemical potential. The biggest merit of considering the finite θ_l region is that there is no sign problem. Indeed, Eq. (1.35) ensures the relation

$$(\mathcal{M}(i\theta_l T, i\theta_l T, 0))^\dagger = \gamma_5\mathcal{M}(i\theta_l T, i\theta_l T, 0)\gamma_5, \tag{1.36}$$

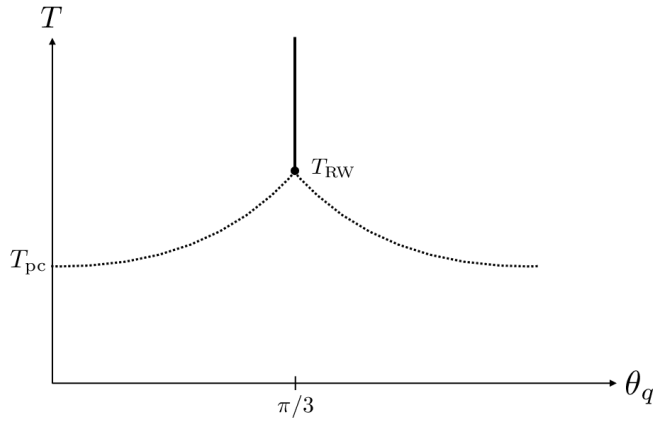

Figure 1.4: Sketch of the phase diagram in T-θ_l plane. The symbols $T_{\rm pc}, T_{\rm RW}$ mean the deconfinement transition temperature at $\theta_l = 0$, the RW transition temperature at $\theta_l = \pi/3$, respectively. The solid vertical line is the RW transition line and the dotted line stands for the crossover deconfinement transition line.

and the fermion determinant has positivity. Therefore, the integrand of $Z_{\rm QCD}$ can be interpreted as a probability function, and the usual Monte-Carlo technique works well. Then, we can obtain the θ_l dependence of physical quantity $\mathcal{O}$ from LQCD simulations. The real μ_l dependence of $\mathcal{O}$ is deduced from the analytic continuation, i.e., by replacing θ_l by $\mu_{\rm l}/T$. This is the basic strategy of the imaginary chemical potential method. When performing the analytic continuation, analyticity of all physical quantities is assumed. It is thus important to know how broad the analytic region is in the finite θ_l region.

Analyses on the finite θ_l region were firstly performed by Roberge and Weiss in Ref. [38]. They showed that $Z_{\rm QCD}$ has the periodicity of $2\pi/3$, that is now called Roberge-Weiss (RW) periodicity. It was also proved by Roberge and Weiss that for $T < T_{\rm pc}$ the thermodynamic quantity is a smooth function of θ_q, while the first-order phase transition takes place at $\theta_q = (2k-1)\pi/3$ for $T > T_{\rm pc}$, where $T_{\rm pc}$ is deconfinement-transition temperature at $\theta_q = 0$. This first-order transition is called the Roberge-Weiss (RW) phase transition. The phase diagram and the quantity deduced from $Z_{\rm QCD}$ thus become periodic in the θ_q region and have singularity at $\theta_q = (2k-1)\pi/3$; See Fig. 1.4 for a sketch of the phase diagram. The available region to the analytic continuation is thus limited to $[0, \pi/3]$, due to the RW phase transition for $T > T_{\rm pc}$ and the RW periodicity for $T < T_{\rm pc}$. Then, the imaginary chemical potential method enables us to extract the real μ_l/T dependence of physical quantity up to the region $\mu_l/T \sim 1$, with small error bars.

To investigate $\mu_l \gtrsim 1$, we can consider effective models, but we need to fix a parameter in the models. In virtue of small error bars, LQCD data

obtained by using the imaginary chemical potential method have a potential to determine a parameter sharply. In particular, the determination of the strength $G_{\rm v}$ of the vector-type four-quark interaction

$$-G_{\rm v}(\bar{q}\gamma_\mu q)^2 \tag{1.37}$$

is important, since the location of the hadron-quark phase transition line is sensitive to its strength $G_{\rm v}$. In Chapter 2, we try to determine the value of $G_{\rm v}$ from LQCD data on the light-quark number density calculated by the imaginary chemical potential method.

1.4.2 Region (B): 2+1-flavor case

Next, let us consider the imaginary chemical potential method for the 2+1-flavor case. In this case, the s-quark chemical potential $\mu_{\rm s}$ is newly introduced as an external parameter, in addition to the light-quark chemical potential. Even for the 2+1-flavor case, the fermion determinant still possesses positivity for $\mu_l = i\theta_l T$ and $\mu_{\rm s} = i\theta_{\rm s} T$, because

$$(\mathcal{M}(i\theta_l T, i\theta_l T, i\theta_{\rm s} T))^\dagger = \gamma_5 \mathcal{M}(i\theta_l T, i\theta_l T, i\theta_{\rm s} T)\gamma_5. \tag{1.38}$$

Hence, the method is useful and applied to the 2+1-flavor case, such as in Refs. [39, 40, 41].

The different point from the 2-flavor case is that the RW periodicity can be lost in the 2+1-flavor case, as shown in Chapter 3. The lack of the periodicity depends on the choice of imaginary $\theta_{\rm s}$. In Ref. [39], Bonati *et al.* showed that the RW periodicity does not exist when $\theta_l \neq 0$ and $\theta_{\rm s} = 0$, by calculating the thermodynamic potential in the high-T limit perturbatively. They also presented a possible phase diagram in T-θ_l plane, illustrated in Fig. 1.5. In Fig 1.5, it should be noted that the first-order phase transition occurs at $\theta_l > \pi/3$, i.e., the transition is delayed when $\theta_{\rm s} = 0$, compared with the 2-flavor case. This indicates that the analytic region can be expanded by breaking the periodicity deliberately and makes the analytic continuation more informative. It is thus interesting to explore when the periodicity is lost, how the actual phase structure is, and how broad the analytic region is. In Chapter 3, we discuss these questions.

1.4.3 Region (C): 2-flavor case with finite isospin chemical potential

We return to the 2-flavor case and consider finite isospin chemical potential $\mu_{\rm iso}$. In this case, u- and d-quarks are not degenerate any more and these chemical potentials $\mu_{\rm u}$ and $\mu_{\rm d}$ are given by

$$\mu_{\rm u} = \mu_l + \mu_{\rm iso}, \quad \mu_{\rm d} = \mu_l - \mu_{\rm iso}. \tag{1.39}$$

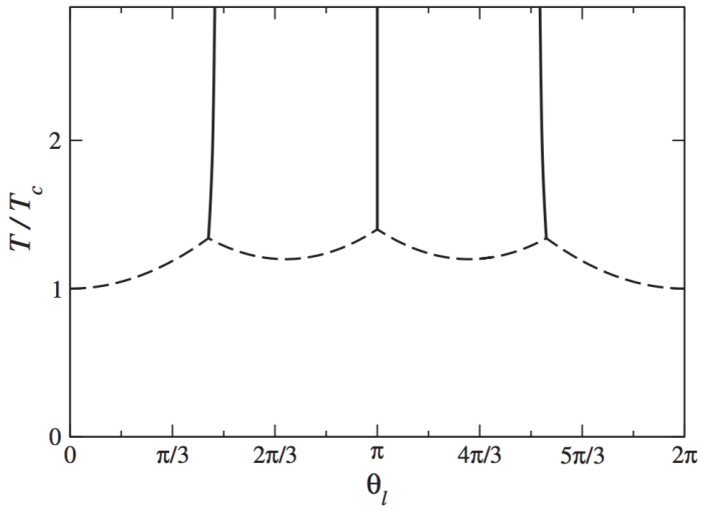

Figure 1.5: The predicted phase diagram in T-θ_l plane in the 2+1-flavor QCD. Figure is taken from Ref. [39].

For $\mu_{\rm iso} = 0$, the relation $\mu_l = \mu_{\rm u} = \mu_{\rm d}$ is then recovered, i.e., the system returns to the 2-flavor case. When $\mu_{\rm iso}$ is finite, the number densities of u- and d-quark are unbalance. This situation can be realized in the inner core of neutron star, where the number density of d-quark is larger than that of u-quark due to the charge neutral condition.

The fermion matrix with finite $\mu_{\rm iso}$ is obtained as

$$\mathcal{M}(\mu_l, \mu_{\rm iso}) = \gamma_\mu D_\mu + \hat{m} - \mu_l \gamma_4 - \mu_{\rm iso}\gamma_4 \tau^3, \tag{1.40}$$

where τ^3 is the third component of the Pauli matrix. We first set $\mu_l = 0$ for simplicity and consider real $\mu_{\rm iso}$. Equation (1.40) with $\mu_l = 0$ does not satisfy the usual γ_5-hermiticity, but for the case of $m_u = m_d = m_l$, the new relation

$$(\mathcal{M}(0, \mu_{\rm iso}))^\dagger = \tau^a \gamma_5 \mathcal{M}(0, \mu_{\rm iso}) \gamma_5 \tau^a, \quad a = 1, 2 \tag{1.41}$$

guarantees that the fermion determinant $\det\mathcal{M}(0, \mu_{\rm iso})$ has positivity. Here, τ^a is the first or second components of the Pauli matrix that anticommutes with τ^3.

Positivity of the fermion determinant makes LQCD simulations feasible. Indeed, some works were performed with LQCD simulations at finite real $\mu_{\rm iso}$ [42, 43]. However, Son and Stephanov demonstrated in Ref. [44] that the charged-pion condensate takes place at $\mu_{\rm iso} = m_\pi/2$ with the pion mass $m_\pi \sim 138$ MeV at vacuum, by using QCD inequalities [45, 46, 47, 48, 12, 49, 50, 51, 52]. Furthermore, it was suggested in Refs. [53, 54] that the charged-pion condensate is related to the severity of the sign problem. LQCD simulations with finite $\mu_{\rm iso}$ are thus difficult to work when the charged-pion condensate occurs.

On the contrary, there is no pion condensate at the imaginary $\mu_{\rm iso}$ region shown in Ref. [55], applying the chiral perturbation theory. LQCD simulations can also be handled in the imaginary $\mu_{\rm iso}$ region, because of no sign problem there; see Refs. [56, 57]. However, there is no discussion on how the γ_5-hermiticity and QCD inequalities are modified, compared with the case of real $\mu_{\rm iso}$. In addition, contributions of μ_l are not included in Refs. [44, 55]. Chapter 4 is devoted to the discussion of the pion condensate not only with real and imaginary $\mu_{\rm iso}$ but also with imaginary μ_l.

1.5 Purpose

The purpose of this thesis is summarized as follow:

- In region (A), the strength $G_{\rm v}$ of the vector-type four-quark interaction is determined from LQCD data on the light-quark number density calculated with the imaginary chemical potential method. Furthermore, we study the impact of $G_{\rm v}$ on neutron-star masses and the hadron-quark phase transition line. These analyses will be done in Chapter 2.

- In region (B), properties of the QCD with imaginary μ_l and $\mu_{\rm s}$ are investigated. We first study the condition needed to realize the RW periodicity, inversely, the condition to break the periodicity. After this, we introduce the effective model that possesses the same properties as the QCD. By using the model, we discuss how largely the analytic region can be expanded. These analyses will be performed in Chapter 3.

- In region (C), it is demonstrated that the charged-pion condensate does not occur. In the proof, QCD inequalities are used. In particular, we clarify what determines the presence or absence of the condensate. The proof will be shown in Chapter 4.

Finally, Chapter 5 is devoted to a summary.

Chapter 2

Hadron-quark phase transition line

2.1 Introduction

In this chapter, we analyze the hadron-quark phase transition line in the QCD phase diagram for the 2-flavor case, constructing reliable effective models. As a model of the quark phase, we use the 2-flavor entanglement PNJL (EPNJL) model [58], which well reproduces LQCD results not only at $\mu_l/T = 0$ but also at imaginary μ_l. Therefore, the EPNJL model is a good starting point. Typically, the EPNJL model is composed of the quark part with the scalar-type four-point interaction and the gluon part described by the Polyakov-loop potential. To analyze the hadron-quark phase transition line at high μ_l, in addition, it is essential to take into account a vector-type four-point interaction with the strength $G_{\rm v}$, since the interaction largely affects on properties of the quark matter there. If we include the vector-type interaction into the model, the strength $G_{\rm v}$ becomes an undetermined parameter. Therefore, we first determine the value of $G_{\rm v}$ at $\mu_l = 0$ from LQCD data on the T dependence of the quark number density [59].

The EPNJL model works well to describe not only the quark phase but also the mesonic degree of freedom [60, 61, 62, 63, 64], while cannot treat the baryonic degree of freedom. Therefore, we adopt the two-phase model approach [65, 66] in which the baryonic model is introduced independently. The two models are connected so as to preserve thermodynamic consistency. Determination of reliable baryonic model is made from whether the adopted model can reproduce the experimental value of the saturation properties and the observed neutron-star mass with two-solar-mass ($2M_\odot$) [32, 33]. By using the obtained two-phase model, we draw the hadron-quark phase transition line and discuss what can be deduced if we assume that the quark matter exists in the $2M_\odot$ neutron stars.

2.2 EPNJL model with vector-type interaction

We first formulate the EPNJL model with the vector-type four-quark interaction. The Lagrangian in Euclidean space-time is defined as

$$\begin{aligned}\mathcal{L}_{\rm EPNJL} =&\bar{q}(\gamma_\mu D_\mu + m_l)q + \mathcal{U}(\Phi,\bar{\Phi}) \\ &- G_{\rm s}(\Phi,\bar{\Phi})[(\bar{q}q)^2 + (\bar{q}i\gamma_5\vec{\tau}q)^2] + G_{\rm v}(\Phi,\bar{\Phi})(\bar{q}\gamma_\mu q)^2, \end{aligned} \tag{2.1}$$

where $q = ({\rm u},{\rm d})^{\rm T}$ is the quark field, $D_\mu = \partial_\mu + iA_\mu\delta_{\mu 4}$ is the covariant derivative, and $G_{\rm s}(\phi,\bar{\phi})$ and $G_{\rm v}(\phi,\bar{\phi})$ are the strength of the scalar- and vector-type interactions with the entanglement vertex [58, 67]:

$$G_{\rm s}(\Phi,\bar{\Phi}) = G_{\rm s}\left[1 - \alpha_1\Phi\bar{\Phi} - \alpha_2(\Phi^3 + \bar{\Phi}^3)\right], \tag{2.2}$$

$$G_{\rm v}(\Phi,\bar{\Phi}) = G_{\rm v}\left[1 - \alpha_1\Phi\bar{\Phi} - \alpha_2(\Phi^3 + \bar{\Phi}^3)\right]. \tag{2.3}$$

In these expressions, α_1 and α_2 denote entanglement parameters. In this thesis, we set $\alpha_1 = \alpha_2 = 0.2$.

For the Polyakov-loop potential $\mathcal{U}(\Phi,\bar{\Phi})$, we use the logarithmic type [**?**, 68]:

$$\mathcal{U}(\Phi,\bar{\Phi}) = T^4\left[-\frac{a(T)}{2}\Phi\bar{\Phi} + b(T)\log H(\Phi,\bar{\Phi})\right], \tag{2.4}$$

where

$$a(T) = a_0 + \left(\frac{T_0}{T}\right) + a_2\left(\frac{T_0}{T}\right)^2, \quad b(T) = b_3\left(\frac{T_0}{T}\right)^3 \tag{2.5}$$

$$H(\Phi,\bar{\Phi}) = 1 - 6\Phi\bar{\Phi} + 4(\Phi^3 + \bar{\Phi}^3) - 3(\Phi\bar{\Phi})^2. \tag{2.6}$$

In the potential $\mathcal{U}(\Phi,\bar{\Phi})$, the parameter T_0 is originally taken to be 270 MeV. This value, however, cannot reproduce LQCD prediction [22, 69] in which the chiral transition temperature T_σ and the deconfinement transition temperature T_Φ almost coincide with each other, $T_\sigma \sim T_\Phi = T_{\rm pc}$, at $\mu_l = 0$. We thus rescale T_0 from 270 MeV to 190 MeV. Under this rescale, the EPNJL model predicts that the chiral and deconfinement transitions take place simultaneously, which is consistent with LQCD data. In Table 2.1, we tabulate the parameters in the EPNJL model.

We comment on the μ_l dependence of T_0. In Ref. [70], it is shown by using the quark-meson model and the functional renormalization group method that T_0 depends on μ_l as

$$\begin{aligned} &T_0(\mu_l) = T_\tau \exp\left[-\frac{1}{\alpha_0 b(\mu_l)}\right], \\ &b(\mu_l) = \frac{29}{6\pi} - \frac{32\mu_l^2}{\pi T_\tau^2}, \quad \alpha_0 = 0.304, \quad T_\tau = 1.770({\rm GeV}). \end{aligned} \tag{2.7}$$

Table 2.1: The parameters included in the Polyakov-loop potential. The value of T_0 is rescaled from the original value 270 MeV to 190 MeV. The other parameters are taken from Ref. [68].

a_0	a_1	a_2	b_3	T_0 [MeV]
3.51	-2.47	15.2	-1.75	190

This represents the backreaction of the quark sector to the gluon sector. However, the phase structure is not changed qualitatively [71] even if we take into account the dependence. We thus treat T_0 as a constant in this thesis.

2.2.1 Thermodynamic potential of EPNJL model

Now, let us perform the mean-field approximation (MFA) to the Lagrangian (**??**). We first decompose the bilinear $A = \bar{q}\Gamma q$ into the expectation value $\langle A\rangle$ and its fluctuation δ_A around $\langle A\rangle$ as

$$A = \langle A\rangle + \delta_A, \tag{2.8}$$

where $\Gamma = 1, i\gamma_5\vec{\tau}, \gamma_\mu$. In the MFA, up to the first order of δ_A is taken into account:

$$\begin{aligned} A^2 &\sim \langle A\rangle^2 + 2\delta_A \langle A\rangle \\ &= \langle A\rangle^2 + 2\langle A\rangle (A - \langle A\rangle) \\ &= 2\langle A\rangle A - \langle A\rangle^2 . \end{aligned} \tag{2.9}$$

Furthermore, the rotational invariance in three-dimensional space yields the relation $\bar{q}\gamma_\mu q = \delta_{\mu 4}\bar{q}\gamma_4 q = \delta_{\mu 4} q^\dagger q$, and the parity invariance of vacuum leads to $\langle \bar{q} i\gamma_5\vec{\tau} q\rangle = 0$ [1)]. The bilinear included in the Lagrangian (**??**) thus become

$$(\bar{q}q)^2 = 2\sigma\bar{q}q - \sigma^2, \quad (\bar{q}i\gamma_5\vec{\tau}q)^2 = 0, \quad (\bar{q}\gamma_\mu q)^2 = 2n_l q^\dagger q - n_l^2. \tag{2.10}$$

Here, $\sigma = \langle \bar{q}q\rangle$ is the chiral condensate and $n_l = \langle q^\dagger q\rangle$ is the quark number density of the light quark.

By using Eq. (2.10), we can reach the Lagrangian under the MFA:

$$\mathcal{L}^{\rm MFA}_{\rm EPNJL} = \bar{q}(\gamma_\mu D_\mu + M_l)q + \mathcal{U}(\Phi, \bar{\Phi}) + G_{\rm s}(\Phi, \bar{\Phi})\sigma^2 - G_{\rm v}(\Phi, \bar{\Phi})n_l^2, \tag{2.11}$$

where $M_l = m_l - 2G_{\rm s}(\Phi, \bar{\Phi})\sigma$ is the constituent quark mass. Substituting the Lagrangian (2.11) for Eq. (1.24) and using Eq. (1.28), we can obtain the

[1)] When we consider the isospin chemical potential $\mu_{\rm iso}$, $\langle \bar{q}i\gamma_5\vec{\tau}q\rangle$ becomes non-zero for $\mu_{\rm iso} \geq m_\pi/2$ with the pion mass m_π at vacuum. See Refs. [55, 58, 71, 72] for the model analyses under finite $\mu_{\rm iso}$.

Table 2.2: The values of Λ, m_l, and $G_{\rm s}$ in the NJL part. The actual values are taken from Ref. [61].

Λ [MeV]	m_l [MeV]	$G_{\rm s}$ [GeV^{-2}]
631.5	5.5	5.498

thermodynamic potential (per unit volume) as

$$\begin{aligned}\Omega_{\rm EPNJL} =& U_{\rm M} + \mathcal{U} - 2\sum_{i={\rm u,d}}\int\frac{d^3\boldsymbol{p}}{(2\pi)^3}\Big[3E \\ &+ \frac{1}{\beta}\log\left(1+3(\Phi+\bar{\Phi}e^{-\beta(E-\tilde{\mu}_i)})e^{-\beta(E-\tilde{\mu}_i)}+e^{-3\beta(E-\tilde{\mu}_i)}\right) \\ &+ \frac{1}{\beta}\log\left(1+3(\bar{\Phi}+\Phi e^{-\beta(E+\tilde{\mu}_i)})e^{-\beta(E+\tilde{\mu}_i)}+e^{-3\beta(E+\tilde{\mu}_i)}\right)\Big], \end{aligned} \tag{2.12}$$

where $\beta = 1/T$ and

$$\begin{aligned} U_{\rm M} &= G_{\rm s}(\Phi,\bar{\Phi})\sigma^2 - G_{\rm v}(\Phi,\bar{\Phi})n_q^2, \\ E &= \sqrt{\boldsymbol{p}^2+M^2}, \\ \tilde{\mu}_i &= \mu_i - 2G_{\rm v}(\Phi,\bar{\Phi})n_l, \end{aligned} \tag{2.13}$$

respectively. The effect of the vector-type interaction is thus incorporated through the shift of μ_i and its magnitude is proportional to n_l.

The vacuum term in Eq. (2.12) diverges in the limit $|\boldsymbol{p}| \to \infty$. We thus apply the three-dimensional cutoff scheme to reguralize the term in which the upper bound of the momentum integral is limited by the parameter Λ. Then, the vacuum term becomes

$$\int\frac{d^3\boldsymbol{p}}{(2\pi)^3}E \;\to\; \int_{|\boldsymbol{p}|\le\Lambda}\frac{d^3\boldsymbol{p}}{(2\pi)^3}E \tag{2.14}$$

and converges [2)]. The introduced parameter Λ is fixed so as to reproduce experimental values of the pion mass and its decay constant, together with m_l and $G_{\rm s}$. The actual values are tabulated in Table 2.2. The strength $G_{\rm v}$ is determined in the next subsection.

The variables $X = \sigma, \Phi, \bar{\Phi}, n_l$ are determined from the stationary condition of

$$\frac{\partial\Omega_{\rm EPNJL}}{\partial X} = 0. \tag{2.15}$$

The stationary condition for n_l yields

$$\begin{aligned} n_l = 6\sum_{i={\rm u,d}}\int\frac{d^3\boldsymbol{p}}{(2\pi)^3}\Big\{&\frac{\Phi{\rm e}^{-\beta(E-\tilde{\mu}_i)}+2\bar{\Phi}{\rm e}^{-2\beta(E-\tilde{\mu}_i)}+{\rm e}^{-3\beta(E-\tilde{\mu}_i)}}{1+3\Phi{\rm e}^{-\beta(E-\tilde{\mu}_i)}+3\bar{\Phi}{\rm e}^{-2\beta(E-\tilde{\mu}_i)}+{\rm e}^{-3\beta(E-\tilde{\mu}_i)}} \\ &-(\Phi\leftrightarrow\bar{\Phi},\quad\tilde{\mu}_i\leftrightarrow-\tilde{\mu}_i)\Big\}. \end{aligned} \tag{2.16}$$

[2)] We do not introduce the cutoff parameter Λ to the momentum integral in the thermal term. As for the model including Λ in the thermal term, see Ref. [74].

It is seen that n_l is a function of $\tilde{\mu}_i$ and hence sensitive to the value of $G_{\rm v}$. This is the reason why the value of $G_{\rm v}$ can be determined by LQCD data on n_l sharply.

Finally, we adopt the approximation $\Phi = \bar{\Phi}$ for the Polyakov loop and its validity has been confirmed in Ref. [58, 73]. If we use this approximation, the condition (2.15) for $\bar{\Phi}$ is not needed. We determine n_l by solving Eq. (2.16) self-consistently, while the other variables σ, Φ are numerically evaluated.

2.2.2 Determination of the value of $G_{\rm v}$

Now, we move to pin down the value of $G_{\rm v}$. Considering the chiral symmetry restored phase, i.e., $T > T_{\rm pc}$, we can show that the chiral condensate σ is nearly equal to zero and thereby the scalar-type interaction becomes negligible. Only the vector-type interaction thus survives as the four-point interaction, and the value of $G_{\rm v}$ can be determined sharply at $T > T_{\rm pc}$.

There is another advantage to focus on the chiral symmetry restored phase. In Ref. [59], the n_l were calculated from LQCD simulations with the imaginary μ_l method. In the actual simulations, a Wilson-type fermion was used as an action for the quark, and the current-quark mass are thus much heavier ~ 130 MeV than the realistic value (~ 5 MeV). In the high-T region, contributions of the current-quark mass can be ignored since the ratio m_l/T becomes small. Therefore, we can obtain the value of $G_{\rm v}$, not depending on m_l there.

To extract the value of $G_{\rm v}$ at $\mu_l = 0$, we define a quantity $n_l/n_{\rm SB}$ with the quark number density $n_{\rm SB}$ in the Stefan-Boltzmann limit:

$$n_{\rm SB} = 2(T^2\mu_l + \mu_l^3). \tag{2.17}$$

The quantity $n_l/n_{\rm SB}$ is μ_l-even. Figure 2.1 presents the T dependence of $n_l/n_{\rm SB}$. In the model calculations, we refit m_l to 130 MeV to match LQCD setup in Ref. [59]. We also plot LQCD data taken from Ref. [75] for the comparison. Note that the error bars are quite small in the imaginary chemical potential method. The value $G_{\rm v} = 0.36G_{\rm s}$ (solid line) yields good agreement between the model result and LQCD data. This value is consistent with the one obtained in Ref. [76] in which the vector-type interaction was determined so as to reproduce the deconfinement transition line in the imaginary μ_l region. If we do not consider the vector-type interaction, then the model calculation largely overestimates LQCD data (dot-dashed line). Meanwhile, the underestimated result is obtained for the case without the entanglement vertex (dashed line). It is thus found that the vector-type interaction and the entanglement vertex are essential.

The dotted line presents the model result with $m_l = 5.5$ MeV. As expected, this result almost agrees with the solid-line one. Therefore, the value $G_{\rm v} = 0.36G_{\rm s}$ is reliable even at $m_l = 5.5$ MeV, although the value is determined by LQCD data obtained at unphysical point.

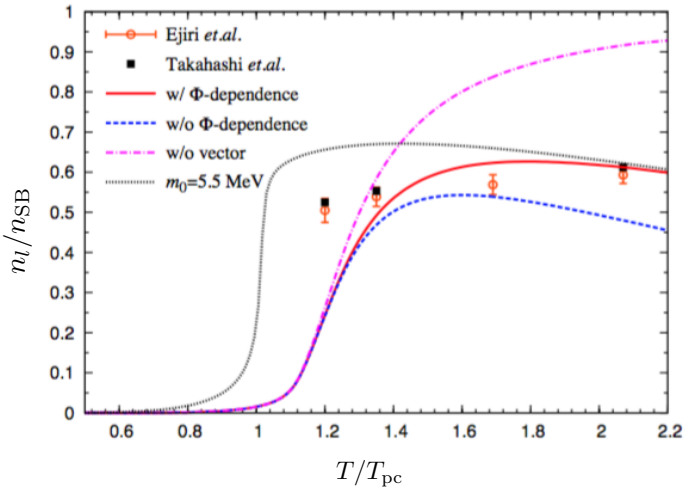

Figure 2.1: Temperature dependence of $n_l/n_{\rm SB}$ at $\mu_l = 0$. The temperature T is normalized by $T_{\rm pc} = 171$ MeV. LQCD data are taken from Refs. [59, 75]. The lines mean the EPNJL model calculations with $G_{\rm v}(\Phi, \bar{\Phi})$ (solid), $G_{\rm v}$ (dashed), and without the vector-type interaction (dotted-dashed), respectively. In these calculations, m_l is fitted to 130 MeV. On the other hand, the dotted line denotes the result with $m_l = 5.5$ MeV.

2.3 Relativistic mean field theory

In the two-phase model approach, we need to use another method to describe the hadron phase realized in the low-T and -μ_l region. So far, various methods were developed for the treatment of the hadron phase; for the low-T region, e.g., we can consider the Brueckner-Hartree-Fock theory [77, 78], its relativistic version [79], the variational method [80, 81, 82, 83], and the relativistic mean field (RMF) theory [84, 85]. As for the high-T and low-μ_l region, the hadron-resonance-gas model quantitatively reproduces LQCD results on some thermodynamic quantities [26, 86, 87, 88]. Among these methods, we take the RMF theory, since it is easy to treat. This also allows us to describe properties of the nuclear matter near the normal nuclear density ρ_0 quantitatively.

The RMF theory is constructed on the basis of the one-meson exchange picture and the Lorentz invariance is imposed on its Lagrangian. The Lagrangian of the RMF theory in Minkowski space-time is defined by

$$\begin{aligned}\mathcal{L}_{\rm RMF} =& \bar{\psi}(i\gamma^\mu\partial_\mu - m_{\rm N} - g_\varphi\varphi - g_\omega\gamma^\mu\omega_\mu - g_\rho\gamma^\mu\rho^a_\mu\tau_a)\psi \\ &+ \frac{1}{2}\partial^\mu\varphi\partial_\mu\varphi - \frac{1}{2}m_\varphi^2\varphi^2 - \frac{1}{3}g_2\varphi^3 - \frac{1}{4}g_3\varphi^4 \\ &- \frac{1}{4}\Omega^{\mu\nu}\Omega_{\mu\nu} + \frac{1}{2}m_\omega^2\omega^\mu\omega_\mu + \frac{1}{4}c_3(\omega^\mu\omega_\mu)^2 - \frac{1}{4}R^{\mu\nu}_a R^a_{\mu\nu} + \frac{1}{2}m_\rho^2\rho^\mu_a\rho^a_\mu,\end{aligned} \tag{2.18}$$

where ψ is the nucleon (N) field, $\Omega^{\mu\nu}$ and $R_a^{\mu\nu}$ are the field strength of ω, ρ mesons, respectively. The mass of each particle is represented by $m_{\rm i}$ with $i = {\rm N}, \varphi, \omega, \rho$. The Yukawa-coupling constants are denoted by $g_\varphi, g_\omega, g_\rho$ and self-interaction constants of φ and ω mesons are by g_2, g_3 and c_3. In Table **??**, we present the interaction channel that each meson mediates.

2.3.1 Thermodynamic potential of RMF theory

We apply the MFA to the RMF theory and derive the expression of the thermodynamic potential. Under the MFA, the meson fields are replaced by the expectation values,

$$\varphi \to \langle\varphi\rangle\,, \quad \omega_\mu \to \langle\omega_0\rangle\,\delta_{\mu 0}, \quad \rho_\mu^a \to \langle\rho_0^3\rangle\,\delta_{\mu 0}\delta^{a3}. \tag{2.19}$$

Here, we have used the rotational invariance in the three-dimensional and the isospin spaces. In the following, we simply denote the expectation values as φ, ω, ρ, respectively. The (expectation values of) meson fields obey the equations

$$\begin{aligned} &m_\varphi^2\varphi + g_2\varphi^2 + g_3\varphi^3 = -g_\varphi\rho_{\rm s}, \\ &m_\omega^2\omega + c_3\omega^3 = g_\omega\rho_{\rm B}, \\ &m_\rho^2\rho = g_\rho\rho_{\rm I}, \end{aligned} \tag{2.20}$$

where $\rho_{\rm s}, \rho_{\rm B}, \rho_{\rm I}$ are the scalar, baryon, and isospin densities, respectively. The relations $\rho_{\rm B} = \rho_p + \rho_{\rm n}$ and $\rho_{\rm I} = \rho_{\rm p} - \rho_{\rm n}$ are satisfied for proton and neutron densities. The former is the baryon number density and the latter is the isospin number density.

The thermodynamic potential (per unit volume) is given by

$$\Omega_{\rm RMF} = U_{\rm meson} - \frac{2}{\beta}\sum_{i={\rm p,n}}\int\frac{d^3\boldsymbol{p}}{(2\pi)^3}\Big[\log(1+{\rm e}^{-\beta(E-\tilde{\mu}_i)}) + \log(1+{\rm e}^{-\beta(E+\tilde{\mu}_i)})\Big], \tag{2.21}$$

together with the meson fields determined by Eq. (2.20). In Eq. (2.21),

$$U_{\rm meson} = \frac{1}{2}m_\varphi^2\varphi^2 + \frac{1}{3}g_2\varphi^3 + \frac{1}{4}g_3\varphi^4 - \frac{1}{2}m_\omega^2\omega^2 - \frac{1}{4}c_3\omega^4 - \frac{1}{2}m_\rho^2\rho^2 \tag{2.22}$$

stands for the mesonic potential and $E = \sqrt{\boldsymbol{p}^2 + M_{\rm N}^2}$ with $M_{\rm N} = m_{\rm N} + g_{\rm s}\varphi$. The effective chemical potentials for neutron (n) and proton (p) are $\tilde{\mu}_{\rm n,p} = \mu_{\rm n,p} - g_\omega\omega \pm g_\rho\rho$.

2.3.2 Parameter set and saturation properties

In the RMF theory, there are too many parameter sets [89]. In this thesis, among them, we take three parameter sets of TM1 [90], NL3 [91], and the parameter set [92] proposed by Maruyama, Tatsumi, Endo, and Chiba

Table 2.3: Three parameter sets of RMF theories. The saturation properties predicted by these parameter sets are also summarized. Shown are the saturation density ρ_0, binding energy E_0, incompressibility K, symmetry energy S_0, and the ratio of the effective nucleon mass $M_{\rm N}$ to nucleon mass $m_{\rm N}$.

parameter	MTEC	TM1	NL3
$m_{\rm N}$ [MeV]	938	938	939
m_φ [MeV]	400	511.198	508.194
m_ω [MeV]	783	783	782.501
m_ρ [MeV]	769	770	763
g_φ	6.3935	10.0289	10.217
g_ω	8.7207	12.6139	12.868
g_ρ	4.2696	4.6322	4.474
g_2 [fm^{-1}]	-10.757	-7.2325	-10.431
g_3	-4.0452	0.6183	-28.885
c_3	0	71.3075	0
saturation property	MTEC	TM1	NL3
ρ_0 (fm^{-3})	0.153	0.145	0.148
E_0 [MeV]	-16.3	-16.3	-16.3
K [MeV]	240	281	271
S_0 [MeV]	32.5	36.9	37.4
$M_{\rm N}/m_{\rm N}$	0.78	0.63	0.60

(MTEC). The parameter sets are tabulated in Table 2.3. The saturation properties predicted from these parameter sets are also shown in Table 2.3.

Now, we consider the equation of state (EoS) at $T = 0$ that gives the relation between the energy per nucleon E/A and $\rho_{\rm B}$. Figure 2.2 presents the EoSs derived from three parameter sets. It is found that all the EoSs yield a universal line up to $\rho_{\rm B} \sim \rho_0$, while a remarkable difference is seen for the high density region. This means that the behavior of the EoS at high density cannot be determined from the saturation properties only. Fortunately, a mass-radius (MR) relation of neutron star is sensitive to the EoS there, and hence we can select a preferable EoS from the MR relation obtained by the neutron star observations. In this section, we calculate the MR relations from the three parameter sets and compare them with the observed results [32, 33] and statistically estimated ones [93].

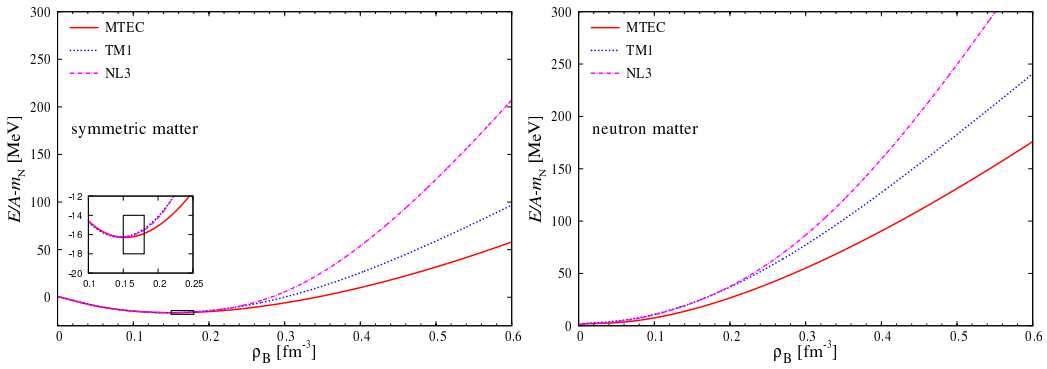

Figure 2.2: The equations of state calculated from three RMF theories. The left panel shows the EoSs for symmetric matter, while the right panel does for neutron matter. In both the panels, the results of MTEC, TM1, and NL3 are denoted by the solid, dotted, and dot-dashed lines, respectively. The open square in the left panel means the empirical saturation point [78].

2.3.3 RMF theory and neutron star observations

The MR relation of neutron star has one-to-one correspondence to the EoS through the Tolman-Oppenheimer-Volkoff (TOV) equation [94]:

$$\frac{dP}{dr} = -G\frac{M\epsilon}{r^2}\left(1+\frac{P}{\epsilon}\right)\left(1+\frac{4\pi Pr^3}{M}\right)\left(1-\frac{2GM}{r}\right)^{-1}, \tag{2.23}$$

$$\frac{dM}{dr} = 4\pi r^2\epsilon, \tag{2.24}$$

where G is the gravitational constant and ϵ is an energy density.

In the inner core of neutron star, the charge-neutral and β-equilibrium conditions should be imposed. The former is described as

$$n_{\rm p} = n_{\rm e} + n_{\mu^-}. \tag{2.25}$$

Here, $n_{\rm e}$ and n_{μ^-} are the number densities of electron and muon, which are treated as massless free particles. The latter condition restricts the number of independent chemical potentials:

$$\mu_i = b_i\mu_{\rm B} - q_i\mu_{\rm e}, \quad i = \left\{{\rm p}, {\rm n}, {\rm e}, \mu^-\right\}, \tag{2.26}$$

where b_i, q_i are the baryon number and the electric charge of each particle and $\mu_{\rm e}$ is an chemical potential of electron. Solving the TOV equation with the EoS that satisfies the conditions (2.25) and (2.26), we can obtain the desired MR relation.

Figure 2.3 presents the obtained MR relations from the three parameter sets. We tabulate the maximum mass ($M_{\rm max}$) and radius ($R_{\rm max}$) in Table 2.4 for each line. In three results, NL3 EoS is too stiff to be consistent with the observational data. On the other hand, MTEC EoS is most consistent with all the data and TM1 EoS is considerably good. In the following, we take MTEC and TM1 as parameter sets of the RMF theory and discard NL3.

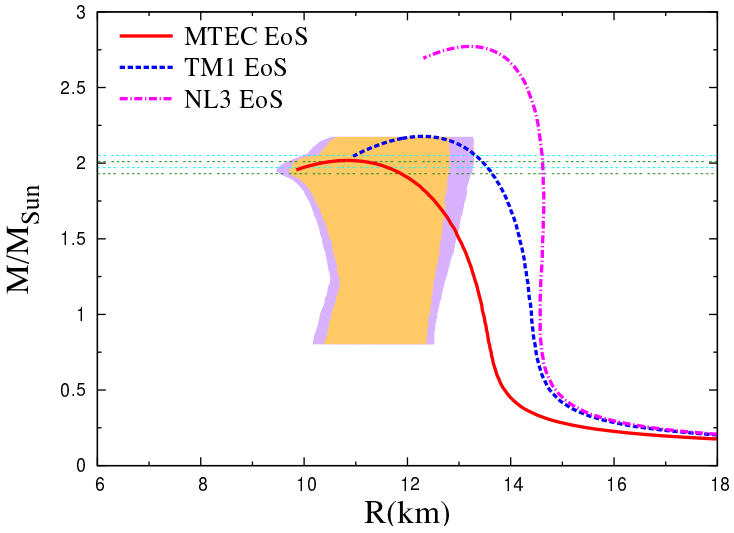

Figure 2.3: MR relations calculated from RMF EoSs with the conditions (2.25) and (2.26). The solid, dotted, and dot-dashed lines correspond to the results for MTEC, TM1, NL3, respectively. The two horizontal boxes denote the $2M_\odot$ observational data reported in Refs. [32, 33]. In addition, the two areas mean the 68% and 95% confidence counters evaluated in Ref. [93].

Table 2.4: The maximum mass ($M_{\rm max}$) and the radius ($R_{\rm max}$) predicted from three RMF models. The mass is normalized by the mass of sun $M_{\rm sun}$.

	MTEC	TM1	NL3
$M_{\rm max}/M_{\rm sun}$	2.02	2.18	2.77
$R_{\rm max}$ [km]	10.8	12.3	13.2

2.4 Two phase model

The EPNJL model is inapplicable for the description of baryonic degree freedom, although it well explains mesonic properties. We therefore take two-phase model approach in which the RMF theory is used for the hadron phase and the EPNJL model for the quark phase. The transition point from the hadron phase to the quark phase is determined by the Gibbs criterion.

Pressures of the RMF theory and the EPNJL model are given by

$$P_{\rm EPNJL}(\mu_{\rm B}, T) = -\left\{\Omega_{\rm EPNJL}(\mu_{\rm B}, T) - \Omega_{\rm EPNJL}(0,0)\right\} - B, \tag{2.27}$$

$$P_{\rm RMF}(\mu_{\rm B}, T) = -\Omega_{\rm RMF}(\mu_{\rm B}, T), \tag{2.28}$$

respectively. We have introduced the bag constant B in Eq. (2.27) in order to describe the difference of vacuums between the hadron phase and the quark phase. The actual value of B is fixed so that the hadron-quark deconfinement transition temperature becomes $T_{\rm pc} = 171$ MeV at $\mu_{\rm B}/T = 0$. From the Gibbs criterion, the hadron phase is realized when $P_{\rm RMF} > P_{\rm EPNJL}$, while

Table 2.5: The label of the two-phase model we consider.

hadron phase	quark phase	label
MTEC	EPNJL model with $G_{\rm v}=0$	TPMa1
MTEC	EPNJL model with $G_{\rm v}=0.36G_{\rm s}$	TPMa2
TM1	EPNJL model with $G_{\rm v}=0$	TPMb1
TM1	EPNJL model with $G_{\rm v}=0.36G_{\rm s}$	TPMb2

the system is in the quark phase for $P_{\rm RMF} < P_{\rm EPNJL}$. With this prescription, $T_{\rm pc} = 171$ MeV is predicted at $\mu_{\rm B}/T = 0$ when we take $B = 100$ MeV^4, even if we use MTEC or TM1 for the hadron phase.

In the Gibbs criterion, the hadron-quark phase transition is the first-order and this order is inconsistent with LQCD prediction in which the transition is crossover at $\mu_{\rm B}/T = 0$ [22]. In the following analyses on neutron star property, we focus on the low-T and high-$\mu_{\rm B}$ region where the hadron-quark phase transition may be the first-order [25]. Our approach is thus valid for the region. See also Refs. [95] on the possibility that the transition is crossover in the low-T and high-$\mu_{\rm B}$.

2.5 Phase transition line without $G_{\rm v}$

In the previous section, we picked up MTEC and TM1 as the RMF theory. Hence, we can take two types of two-phase model; see Table 2.5. Now, we first consider the case of TPMa1 and TPMb1, i.e., the case that the vector-type interaction is switched off, and investigate whether the quark matter exists in the inner core of $2M_\odot$ neutron star. In the EoS of two-phase model, the charge neutral and β-equilibrium conditions are also imposed on the quark phase. The former is given by

$$\mu_{\rm u} = \frac{1}{3}\mu_{\rm B} - \frac{2}{3}\mu_{\rm e}, \quad \mu_{\rm d} = \frac{1}{3}\mu_{\rm B} + \frac{1}{3}\mu_{\rm e}, \tag{2.29}$$

and the latter is by

$$\frac{2}{3}n_{\rm u} - \frac{1}{3}n_{\rm d} - n_{\rm e} - n_{\mu^-} = 0. \tag{2.30}$$

Under the quark-matter EoS and the hadron-matter EoS, the EoS of the two-phase model is constructed according to the Gibbs criteria.

The panel (a) of Fig. 2.4 presents the MR relations of TPMa1 and TPMb1. The results obtained from MTEC and TM1 only are also plotted for the comparison. The Fermi energy decreases when the quark matter appears. Then, the derivative $\partial M/\partial\rho_{\rm B}$, or $\partial M/\partial R$ becomes negative. Indeed, the mass of neutron star starts to decrease at $M = 1.97M_\odot$ for TPMa1

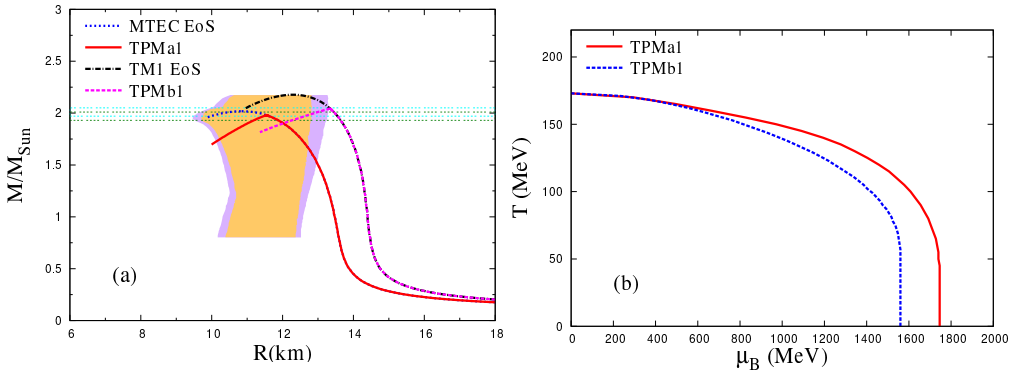

Figure 2.4: (a) The MR relation calculated from TPMa1 and TPMb1. For the comparison, we also plot the results from MTEC and TM1. The meaning of two horizontal boxes and the two areas are the same as in Fig. 2.3. (b) The hadron-quark phase transition line drawn by using TPMa1 and TPMb1. The vertical axis is temperature T and the horizontal axis is the baryon chemical potential $\mu_{\rm B} = 3\mu_l$.

and at $M = 2.04 M_\odot$ for TPMb1, but these values are consistent with the observational data.

The panel (b) of Fig. 2.4 illustrates the hadron-quark phase transition line drawn by TPMa1 and TPMb1 in which the matter is taken to be symmetric, i.e., the number densities of u- and d-quarks (neutron and proton) are equal. The vertical axis is T and the horizontal axis corresponds to baryon chemical potential $\mu_{\rm B} = 3\mu_q$. The critical baryon chemical potential $\mu_{\rm B}^{\rm c}$ at $T = 0$ is 1750 MeV for TPMa1, but 1560 MeV for the TPMb1. If the vector-type interaction switches on, the quark-matter EoS becomes stiff. Therefore, it is predicted that the transition line is shifted toward the high $\mu_{\rm B}$ direction and TPMa1 and TPMb1 yields the lower bound of $\mu_{\rm B}^{\rm c}$ for each class of the two-phase models.

2.6 Effects of $G_{\rm v}$ on hadron-quark transition line

Next, we consider two kinds of two-phase models, TPMa2 and TPMb2, where TPMa2 has no vector-type interaction but TPMb2 has it. In these models, we numerically checked that the quark matter does not take place in the inner core of neutron star, i.e., the pressure of the hadron phase is always larger than that of the quark phase. This fact suggests that the strength $G_{\rm v} = 0.36 G_{\rm s}$ is too strong and a possibility of the existence of the quark phase is excluded.

The hadron-quark phase transition line predicted by TPMa2 is shown in Fig 2.5. From the comparison with the result of the TPMa1, the vector-type

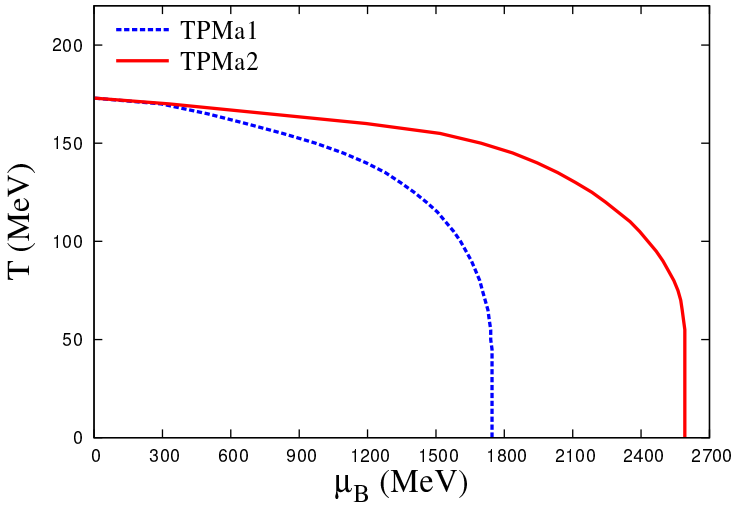

Figure 2.5: The hadron-quark phase transition line calculated by TPMa2.

interaction with the strength $G_{\rm v} = 0.36G_{\rm s}$ largely delays the transition. The critical value $\mu_{\rm B}^{\rm c}$ for TPMa2 is 2600 MeV and the corresponding density is $\rho_{\rm B} \sim 13\rho_0$, where ρ_0 is 0.153fm^{-3}. Such a high density is not realized in the inner core of neutron star. As for TPMb2, we found that the transition line never reach the $\mu_{\rm B}$ axis. In the RMF theory with the TM1 parameter set, the self-interaction $(\omega^\mu\omega_\mu)^2$ of ω-meson makes the hadron phase favor as increasing $\mu_{\rm B}$. Furthermore, the quark phase is more difficult to appear if the vector-type interaction is non-zero. Due to these effects, the transition line cannot reach the $\mu_{\rm B}$ axis.

2.7 Density dependence of $G_{\rm v}$

In the previous section, it was seen that the quark phase does not take place in the inner core of neutron star. The reason is that the vector-type interaction is very strong. In this section, we consider the density-dependent vector-type interaction in which the strength is weaken with $\rho_{\rm B}$.

2.7.1 Density-dependent vector-type interaction

We now introduce the density-dependent vector-type interaction as

$$G_{\rm v}(n_l) = G_{\rm v} \exp\left[-b\left(\frac{n_l}{\rho_0}\right)^2\right], \tag{2.31}$$

where b is a free parameter. The case of $b \to \infty$ corresponds to the EPNJL model without the vector-type interaction, whereas the EPNJL model with $G_{\rm v} = 0.36G_{\rm s}$ is obtained for $b = 0$. The thermodynamic potential is obtained by the replacement $G_{\rm v} \to G_{\rm v}(n_l)$ in Eq. (2.12). By using EPNJL model with Eq. (2.31), we define two types of models presented in Table. 2.6.

Table 2.6: The label of the two-phase model with the density-dependent vector-type interaction.

hadron phase	quark phase	label
MTEC	EPNJL model with $G_{\rm v}(n_l)$	TPMa3
TM1	EPNJL model with $G_{\rm v}(n_l)$	TPMb3

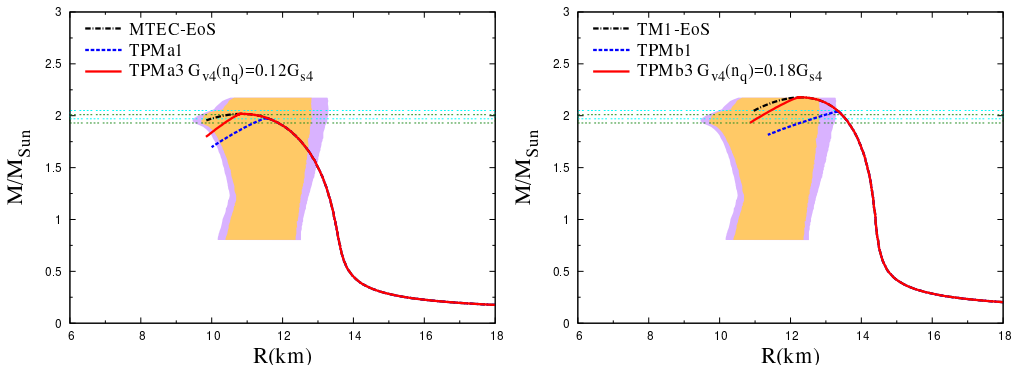

Figure 2.6: The MR relation calculated from TPMa3 (left panel) and TPMb3 (right panel). For TPMa3, $G_{\rm v}(7.2\rho_0) = 0.12G_{\rm s}$ is used and $G_{\rm v}(6\rho_0) = 0.18G_{\rm s}$ for TPMb3.

As already mentioned above, TPMa1 and TPMb1 predict the appearance of the quark matter in the inner core of neutron star, while TPMa2 and TPMb2 do not due to the strong vector-type interaction. This fact indicates that the quark matter can appear at some critical value $b_{\rm c}$ with increasing b. To determine the value of $b_{\rm c}$, we assume that the quark phase is realized in the inner core of stable neutron star. If the quark phase appears in the inner core of neutron star, the mass decreases, i.e., neutron star becomes unstable; see Fig. 2.4. Hence, we search the value of $G_{\rm v}$ and the density when the maximum mass predicted by TPMa3 (TPMb3) coincides with that of MTEC (TM1).

The left panel of Fig. 2.6 shows the MR relation of TPMa3. The quark phase appears at $2.02M_\odot$ and $n_l = 7.2\rho_0$, when we set $G_{\rm v}(7.2\rho_0) = 0.12G_{\rm s}$. This value is the upper value of $G_{\rm v}(n_l)$ when the quark phase is realized in the core of neutron star. By inserting $n_l = 7.2\rho_0$ and $G_{\rm v}(n_l)$ into Eq. (2.31), we can obtain the minimum value of b, i.e., $b_{\rm c} = 0.001$. The right panel is the same as the left panel but TM1 and TPMb3 is taken instead of MTEC and TPMa3. In the case of TPMb3, the maximum mass $2.17M_\odot$ is achieved at $n_l = 6\rho_0$ and $G_{\rm v}(6\rho_0) = 0.18G_{\rm s}$, which leads to $b_{\rm c} = 0.001$. Therefore, the value of $b_{\rm c}$ is common for TPMa3 and TPMb3.

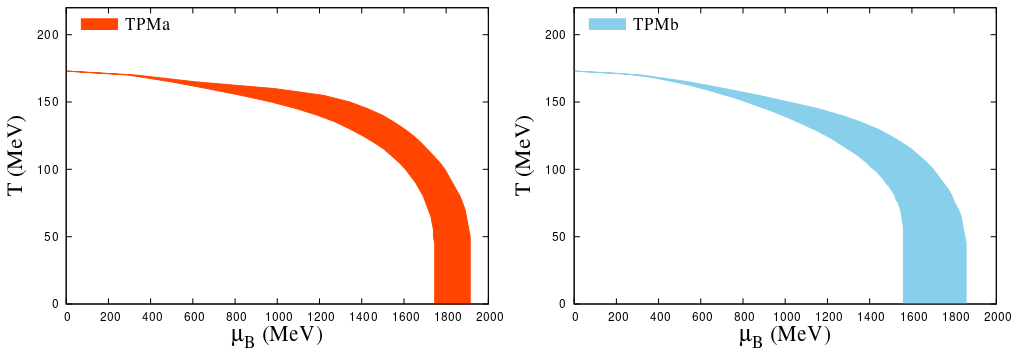

Figure 2.7: The band of the hadron-quark phase transition line predicted by TPMa3 (left panel) and TPMb3 (right panel). In the calculation, we assume that the quark phase exists in the inner core of neutron star.

2.7.2 Hadron-quark phase transition line with $G_{\rm v}(n_l)$

In Fig. 2.7, we draw the hadron-quark phase transition line for symmetric matter. In the left panel, the lower line is obtained from TPMa1, while the upper line is from TPMa3 with $b_{\rm c} = 0.001$. Hence, the transition line should lie within the red band if the quark phase exists in the inner core of neutron star. The right panel presents the same result but the lower line is drawn by TPMb1 and the upper line is by TPMb3 with $b_{\rm c} = 0.001$. The critical baryon chemical potential $\mu_{\rm B}^{\rm c}$ at $T = 0$ is in 1750 MeV $\leq \mu_{\rm B}^{\rm c} \leq$ 1910 MeV for the left panel and in 1560 MeV $\leq \mu_{\rm B}^{\rm c} \leq$ 1860 MeV for the right panel. This indicates that the upper line has little dependence on the parameter set of the RMF theory.

2.8 Short summary

In this chapter, we have investigated the hadron-quark phase transition line based on some two-phase models. For the quark phase, we used the EPNJL model with the vector-type interaction. The strength $G_{\rm v}$ of the vector-type interaction at $\mu_l = 0$ was determined from LQCD data on the quark number density calculated by the imaginary chemical potential method. The obtained value is $G_{\rm v} = 0.36 G_{\rm s}$, where $G_{\rm s}$ is the scalar-type interaction.

As for the hadron phase, the relativistic mean field (RMF) theory was applied with the three parameter sets; TM1 [90], NL3 [91], and MTEC [92]. All the parameter sets yield almost the same equation of state (EoS) for $\rho_{\rm B} \leq \rho_0$. On the contrary, the behavior of the EoS in the large $\rho_{\rm B}$ region is quite different among them. Hence, we calculated the MR relation of neutron star from the three parameter sets and compared with the observational data and the statistically estimated one. We thus selected MTEC and TM1 as suitable parameter sets.

Next, we constructed four two-phase models, i.e., TPMa1, TPMa2, TPMb1,

and TPMb2. By using these models, we calculated the MR relation. Among these models, TPMa1 and TPMb1 predict that the quark phase appears in the inner core of neutron star, while the quark phase is not realized for the other models. As for the hadron-quark phase transition line, the transition point is shifted toward large $\mu_{\rm B}$ direction.

Finally, the density-dependent vector-type interaction was considered. We took a Gaussian form for the density dependence in which one parameter b is introduced. We then constructed TPMa3 and TPMb3, i.e., the density-dependent vector-type interaction is equipped in the quark part. By assuming that the quark phase exists in the inner core of neutron star, we showed that the lower value of b is 0.001 for both TPMa3 and TPMb3. From TPMa1 and TPMa3, the hadron-quark phase transition line was drawn. As a result, the critical baryon chemical potential $\mu_{\rm B}^{\rm c}$ at $T = 0$ lies in the region 1750 MeV $\leq \mu_{\rm B}^{\rm c} \leq$ 1910 MeV, if the quark phase appears in the inner core of neutron star. As for TPMb1 and TPMb3, the obtained result is 1560 MeV $\leq \mu_{\rm B}^{\rm c} \leq$ 1860 MeV. These suggest that the upper value of $\mu_{\rm B}^{\rm c}$ has little dependence on the RMF theory taken.

Chapter 3

2+1-flavor QCD in the imaginary region

3.1 Introduction

In this chapter, we consider the 2+1-flavor QCD in the imaginary chemical potential region, where the light- and s-quark chemical potentials, $\mu_l = i\theta_l T$ and $\mu_{\rm s} = i\theta_{\rm s} T$, are introduced. In this region, the QCD does not encounter the sign problem shown in Eq. (1.38). Therefore, information on finite real $(\mu_l, \mu_{\rm s})$ can be extracted from LQCD simulations, by employing the analytic continuation. Along this strategy, it is important to know the analyticity of the imaginary chemical potential region. For the 2-flavor case, it is well-known that the first-order RW transition takes place at $\theta_l = \pi/3$ and the analyticity is breakdown there. On the contrary, as shown in Ref. [39], the RW transition point is shifted to high θ_l direction when the RW periodicity is broken.

This previous work encourages us to study properties of the QCD in the imaginary chemical potential region, $\mu_l = i\theta_l T$ and $\mu_{\rm s} = i\theta_{\rm s} T$. We clarify conditions imposed on $(\theta_l, \theta_{\rm s})$ to realize the RW periodicity, and inversely, to break the periodicity. Next, we introduce the Polyakov-loop extended Nambu–Jona-Lasinio (PNJL) model [98] that possesses the same properties as the QCD in the $(\theta_l, \theta_{\rm s})$ region. By using the PNJL model, we calculate some thermodynamic quantities and draw the QCD phase diagram, in order to check the prediction of Ref. [39]. We also investigate how the analytic region can be expanded by breaking the RW periodicity. We will show that no first-order transition occurs for some choices of θ_l and $\theta_{\rm s}$.

3.2 RW periodicity in the QCD

We first consider the case that all the imaginary chemical potentials $\mu_f = i\theta_f T$ $(f = {\rm u}, {\rm d}, {\rm s})$ are treated as independent variables. The 2+1-flavor QCD is recovered when we set $\theta_{\rm u} = \theta_{\rm d} = \theta_l$. Our starting point is the grand-

canonical partition function

$$Z_{\rm QCD} = \int \mathcal{D}A\mathcal{D}\bar{q}\mathcal{D}q \exp\left[-S_{\rm QCD}\right] \tag{3.1}$$

with the action

$$S_{\rm QCD} = \int_0^\beta d\tau \int d^3\boldsymbol{x} \left[\bar{q}\left(\gamma_\mu D_\mu + \hat{m} - i\frac{\hat{\theta}}{\beta}\gamma_4\right) q + \frac{1}{2g^2}{\rm Tr_c} F_{\mu\nu}F_{\mu\nu}\right], \tag{3.2}$$

where $\hat{\theta} = {\rm diag}(\theta_{\rm u}, \theta_{\rm d}, \theta_{\rm s})$ is the dimensionless imaginary chemical potential matrix. The definition of the other symbols is the same as in Eq. (1.2). Note that the anti-periodic boundary condition is imposed on the quark fields,

$$q_f(\beta, \boldsymbol{x}) = -q_f(0, \boldsymbol{x}). \tag{3.3}$$

We transform the quark fields as

$$q_f \to \exp\left[i\frac{\theta_f}{\beta}\tau\right] q_f. \tag{3.4}$$

The integral measure in Eq. (3.1) is unchanged, but the action $S_{\rm QCD}$ becomes

$$Z_{\rm QCD} = \int_0^\beta d\tau \int d^3\boldsymbol{x} \left[\bar{q}\left(\gamma_\mu D_\mu + \hat{m}\right) q + \frac{1}{2g^2}{\rm Tr_c} F_{\mu\nu}F_{\mu\nu}\right], \tag{3.5}$$

i.e., the chemical potential term is removed. Instead, the boundary condition of q_f is twisted as

$$q_f(\beta, \boldsymbol{x}) = -{\rm e}^{i\theta_f} q(0, \boldsymbol{x}). \tag{3.6}$$

Now, let us remember the $\mathbb{Z}_3$ transformation generated by Eq. (1.9). The $\mathbb{Z}_3$-transformed quark field satisfies the new boundary condition twisted by an element of the $\mathbb{Z}_3$ group,

$$q_f(\beta, \boldsymbol{x}) = -\exp\left[i\left(\theta_f + \frac{2\pi k}{3}\right)\right] q_f(0, \boldsymbol{x}), \tag{3.7}$$

shown in Eq. (1.17). Here, $k = -1, 0, 1$. In Eq. (3.7), the additional shift $2\pi k/3$ can be compensated by the shift $\theta_f \to \theta_f - 2\pi k/3$, and thereby we can obtain the equality

$$Z_{\rm QCD}(\theta_f + 2\pi k/3) = Z_{\rm QCD}(\theta_f). \tag{3.8}$$

The QCD grand-canonical partition function thus has the periodicity of $2\pi/3$ in θ_f, i.e., the RW periodicity.

From the discussion mentioned above, it is found that the RW periodicity is a consequence of the invariance under the $\mathbb{Z}_3$ transformation and the shift $\theta_f \to \theta_f + 2\pi k/3$. This is called the extended $\mathbb{Z}_3$ transformation [96, 97]. In the 2+1-flavor case, $\theta_{\rm u} = \theta_{\rm d} = \theta_l$, the RW periodicity is seen for the condition $\theta_l = \theta_{\rm s}$. Meanwhile, if we set any one of θ_f to a constant, e.g., $\theta_{\rm s} = 0$ in Ref. [39], the periodicity disappears since the shift of θ_f is unavailable. The thermodynamic potential $\Omega_{\rm QCD}$ of the QCD also has the same properties, because of the relation $\Omega_{\rm QCD} = -T\log Z_{\rm QCD}$. In the next section, we introduce the 2+1-flavor PNJL model.

3.3 2+1-flavor PNJL model

We formulate the 2+1-flavor Polyakov-loop extended Nambu–Jona-Lasinio (PNJL) model [98]. The Lagrangian is defined by

$$\begin{aligned}\mathcal{L}_{\rm PNJL} =&\bar{q}(\gamma_\mu D_\mu + \hat{m})q + \mathcal{U}(\Phi,\bar{\Phi}) - G_{\rm s}\sum_{a=0}^{8}\left[(\bar{q}\lambda^a q)^2 + (\bar{q}i\gamma^5\lambda^a q)^2\right] \\ &+ K\left[\det{}_{f,f'}\bar{q}(1+\gamma_5)q + \det{}_{f,f'}\bar{q}(1-\gamma_5)q\right], \end{aligned} \tag{3.9}$$

where $q = (\mathrm{u},\mathrm{d},\mathrm{s})^{\rm T}$ is the quark field and the mass matrix $\hat{m} = \mathrm{diag}(m_l, m_l, m_s)$ is is composed of the u- and d-quark masses m_l and the s-quark current mass m_s. The covariant derivative D_μ, the Polyakov-loop potential $\mathcal{U}(\Phi,\bar{\Phi})$ have the same form as the 2-flavor case, respectively. The quark fields interact with each other through two-types of interactions; one is the four-point scalar-type interaction and the other is the Kobayashi-Maskawa-'t Hooft (KMT) interaction [2, 3, 99]. The former preserves $\mathrm{U(3)_R}\otimes\mathrm{U(3)_L}$ symmetry, while the latter breaks $\mathrm{U(1)_A}$ symmetry and causes the flavor mixing, which is an essential ingredient to reproduce the mass of η'-meson.

Also for the 2+1-flavor case, we can consider the EPNJL model [102], i.e., the PNJL model with the entanglement vertex in Eq. (2.2). However, the 2+1-flavor EPNJL model cannot explain the weak correlation between the chiral and the deconfinement transitions, suggested by LQCD simulation [24]. At present, there is no effective model that can explain the weak correlation, and hence we perform a qualitative analysis on the 2+1-flavor QCD in the imaginary chemical potential region by using the PNJL model.

3.4 Thermodynamic potential

As for the 2-flavor case, we apply the MFA to the Lagrangian (3.9). For the 2+1-flavor case, we also assume that the pseudo-scalar type condensate does not occur. Furthermore, if we neglect the Fock term and the condensate $\langle\bar{q}_f q_{f'}\rangle$ for $f \neq f'$, the scalar-type interaction is replaced as

$$-G_{\rm s}\sum_{a=0}^{8}\left[(\bar{q}\lambda^a q)^2 + (\bar{q}i\gamma^5\lambda^a q)^2\right] \to -4G_{\rm s}\sum_f \sigma_f\bar{q}_f q_f + 2G_{\rm s}\sum_f \sigma_f^2. \tag{3.10}$$

In the KMT interaction, we have to calculate the determinant in flavor space,

$$\det\begin{pmatrix}\bar{u}\Gamma^{\pm}u & \bar{u}\Gamma^{\pm}d & \bar{u}\Gamma^{\pm}s \\ \bar{d}\Gamma^{\pm}u & \bar{d}\Gamma^{\pm}d & \bar{d}\Gamma^{\pm}s \\ \bar{s}\Gamma^{\pm}u & \bar{s}\Gamma^{\pm}d & \bar{s}\Gamma^{\pm}s\end{pmatrix}, \tag{3.11}$$

for $\Gamma^{\pm} = 1 \pm \gamma_5$. However, by using the assumption employed in the scalar-type interaction, the determinant term becomes simple as

$$K\left[\det{}_{f,f'}\bar{q}(1+\gamma_5)q + \det{}_{f,f'}\bar{q}(1-\gamma_5)q\right] = 2K(\bar{u}u)(\bar{d}d)(\bar{s}s). \tag{3.12}$$

We finally reach the replacement

$$K\Big[\det_{f,f'}\bar{q}(1+\gamma_5)q+\det_{f,f'}\bar{q}(1-\gamma_5)q\Big] \\ \to 2K\sigma_{\rm d}\sigma_{\rm s}\bar{u}u+2K\sigma_{\rm u}\sigma_{\rm d}\bar{s}s+2K\sigma_{\rm u}\sigma_{\rm d}-4K\sigma_{\rm u}\sigma_{\rm d}\sigma_{\rm s}. \tag{3.13}$$

See Appendix C for more detail. Note that $\sigma_{\rm u}=\sigma_{\rm d}=\sigma_l$ in the 2+1-flavor case.

By using Eqs. (3.10) and (3.13), we can obtain the Lagrangian under the MFA as

$$\mathcal{L}^{\rm MFA}_{\rm PNJL}=\bar{q}(\gamma_\mu D_\mu+\hat{M})q+\mathcal{U}(\Phi,\bar{\Phi})+2G_{\rm s}(2\sigma_l^2+\sigma_{\rm s}^2)-4K\sigma_l^2\sigma_{\rm s}, \tag{3.14}$$

where $\hat{M}=\mathrm{diag}(M_l,M_l,M_{\rm s})$ is the constituent quark-mass matrix composed of

$$M_l=m_l-4G_{\rm s}\sigma_l+2K\sigma_l\sigma_{\rm s}, \tag{3.15}$$
$$M_{\rm s}=m_{\rm s}-4G_{\rm s}\sigma_{\rm s}+2K\sigma_l^2. \tag{3.16}$$

Substituting Eq. (3.14) into the expression Eq. (1.24) and using Eq. (1.28), we obtain the thermodynamic potential of the 2+1-flavor PNJL model:

$$\begin{aligned}\Omega_{\rm PNJL}=&U_{\rm M}+\mathcal{U}(\Phi,\bar{\Phi})-2\sum_f\int\frac{d^3\boldsymbol{p}}{(2\pi)^3}\Big[3E_f \\ &+\frac{1}{\beta}\log\left(1+3(\Phi+\bar{\Phi}e^{-\beta(E_f-\mu_f)})e^{-\beta(E_f-\mu_i)}+e^{-3\beta(E_f-\mu_f)}\right) \\ &+\frac{1}{\beta}\log\left(1+3(\bar{\Phi}+\Phi e^{-\beta(E_f+\mu_f)})e^{-\beta(E_f+\mu_i)}+e^{-3\beta(E_f+\mu_f)}\right)\Big].\end{aligned} \tag{3.17}$$

In Eq. (3.17), we have defined the following expressions:

$$U_{\rm M}=2G_{\rm s}\sum_f\sigma_f^2-4K\sigma_{\rm u}\sigma_{\rm d}\sigma_{\rm s}, \tag{3.18}$$
$$E_f=\sqrt{\boldsymbol{p}^2+M_f^2}. \tag{3.19}$$

Also for the 2+1-flavor case, the vacuum term is regularized by the three-dimensional cutoff scheme; see Eq. (2.14).

For the parameter T_0 of the Polyakov-loop potential, we set $T_0=270$ MeV, i.e., the original value in Ref. [68]. The other parameters are the same as in Table 2.1. The parameters in the quark part are determined so as to reproduce the pion, kaon, η' meson masses and the pion decay constant [100]. The parameters thus obtained are tabulated in Table 3.1. Finally, the variables $\Phi,\bar{\Phi},\sigma_l$, and $\sigma_{\rm s}$ are determined from the stationary conditions,

$$\frac{\partial\Omega_{\rm PNJL}}{\partial X},\quad X=\Phi,\bar{\Phi},\sigma_l,\sigma_{\rm s}. \tag{3.20}$$

Table 3.1: The values of $\Lambda, m_l, m_{\rm s}, G_{\rm s}$, and K in the quark part. The values are taken from Ref. [100].

Λ [MeV]	m_l [MeV]	$m_{\rm s}$ [MeV]	$G_{\rm s}\Lambda^2$	$K\Lambda^5$
602.3	5.5	140.7	1.835	12.36

3.5 RW periodicity and its breaking in the PNJL model

To see that Eq. (3.17) has the same properties as the QCD thermodynamic potential clearly, we introduce the flavor-dependent modified Polyakov loop and its conjugate as

$$\Psi_f = {\rm e}^{i\theta_f}\Phi, \quad \bar{\Psi}_f = {\rm e}^{-i\theta_f}\bar{\Phi}. \tag{3.21}$$

These quantities are extended-$\mathbb{Z}_3$ invariant, unlike the Polyakov loop. In Eq. (3.17), the θ_f dependence is embedded in the second and third lines. These can be rewritten by Ψ_f and $\bar{\Psi}_f$ and become

$$\begin{aligned}\frac{1}{\beta}\Big[&\log\left(1+3\Psi_f{\rm e}^{-\beta E_f}+3\bar{\Psi}_f{\rm e}^{-2\beta E_f}{\rm e}^{3i\theta_f}+{\rm e}^{-3\beta E_f}{\rm e}^{3i\theta_f}\right)\\ &+\log\left(1+3\bar{\Psi}_f{\rm e}^{-\beta E_f}+3\Psi_f{\rm e}^{-2\beta E_f}{\rm e}^{-3i\theta_f}+{\rm e}^{-3\beta E_f}{\rm e}^{-3i\theta_f}\right)\Big].\end{aligned} \tag{3.22}$$

The factors depending on θ_f are $\{\Psi_f, \bar{\Psi}_f, {\rm e}^{\pm 3i\theta_f}\}$, i.e., all are the extended-$\mathbb{Z}_3$ invariant. Therefore, the thermodynamic potential $\Omega_{\rm PNJL}$ possesses the RW periodicity in general. Once we fix any one of θ_f, however, the corresponding modified Polyakov loop is not invariant under the extended $\mathbb{Z}_3$ transformation, since $\Psi_f \to \Psi_f {\rm e}^{2\pi ik/3}$. Hence, $\Omega_{\rm PNJL}$ does not show the RW periodicity. It is thus found that $\Omega_{\rm PNJL}$ has the same properties as $\Omega_{\rm QCD}$ on the RW periodicity.

3.6 Numerical results

We present the numerical results calculated from the PNJL model. We first calculate $\Omega_{\rm PNJL}$ and the quark number density n_q under the conditions, (I) $\theta_l = \theta_{\rm s}$ and (II) θ_l is varied with $\theta_{\rm s} = 0$. The QCD phase diagram in the θ_l-T plane is also drawn for conditions (I) and (II). It is found that the RW periodicity preserves for the condition (I), while not for the condition (II). Finally, the u- and s-quark number densities are calculated. For the former, we fix the d- and s-quark chemical potentials, and the u- and d-quark chemical potentials are taken to be constants for the latter. In these situations, we show that no first-order phase transition occurs in the quantities.

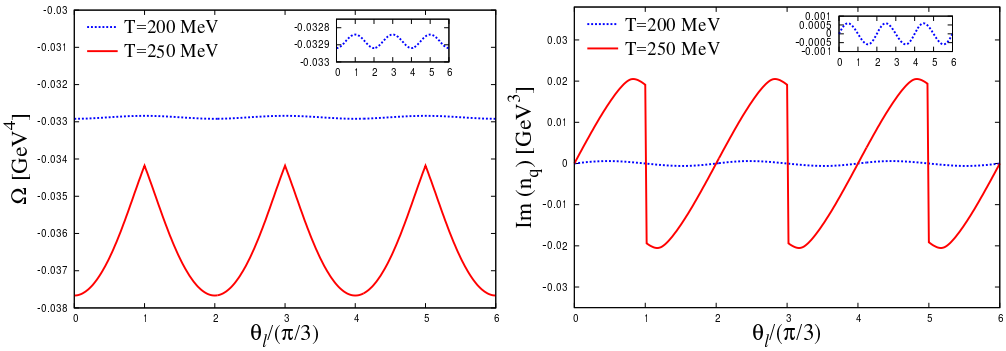

Figure 3.1: The θ_l dependence of $\Omega_{\rm PNJL}$ (left panel) and the imaginary part of n_q (right panel) for condition (I). The dotted line denotes the result with $T = 200$ MeV and the solid line means the one with $T = 250$ MeV.

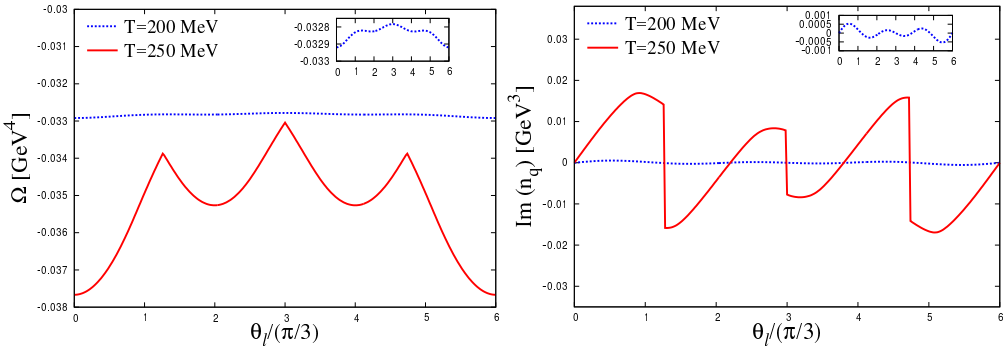

Figure 3.2: The θ_l dependence of $\Omega_{\rm PNJL}$ and the imaginary part of n_q for condition (II). The meaning of the lines is the same as in Fig. 3.1.

3.6.1 Behavior of thermodynamic quantities

The quark number density n_q is defined from $\Omega_{\rm PNJL}$ as

$$n_q = \sum_f n_f = -\sum_f \frac{\partial \Omega_{\rm PNJL}}{\partial \mu_f} = i\beta \sum_f \frac{\partial}{\partial \theta_f} \Omega_{\rm PNJL}, \tag{3.23}$$

where n_f is the number density for each flavor. When $\Omega_{\rm PNJL}$ has the RW periodicity, n_q also does. Note that $\Omega_{\rm PNJL}$ is charge-even and hence n_q is charge-odd.

Figure 3.1 shows the θ_l dependence of $\Omega_{\rm PNJL}$ and the imaginary part of n_q for the condition (I). The dotted line is the result for $T = 200$ MeV and the solid line is for $T = 250$ MeV. Both of them have the RW periodicity, as expected, and are a smooth function of θ_l for $T = 200$ MeV. For $T = 250$ MeV, $\Omega_{\rm PNJL}$ has a cusp structure at $\theta_l = \pi/3$ mod $2\pi/3$, while n_q is discontinuous there. As for the types of the singularities, see Appendix D. These singularities indicate the RW transition and its end point is located in $200 < T < 250$ MeV.

The results for the condition (II) are plotted in Fig. 3.2. The lines are the

same as in Fig. 3.1. The RW periodicity is lost, but the first-order transition, which is the remnant of the RW transition, still occurs. We call it the first-order "RW-like transition". In the region of $0 \leq \theta_l \leq 2\pi/3$, the RW-like transition takes place at $\theta_l = 0.42\pi$, i.e., the point is larger than that of the RW transition point $\theta_l = \pi/3$. Hence, the analytic region becomes broad, as pointed out in Ref. [39].

3.6.2 QCD phase diagram

Next, we aim at drawing the QCD phase diagram for the conditions (I) and (II). To search the RW or RW-like transition points, charge-odd quantity is a good indicator [103], since a discontinuity is seen at the transition points. We thus use n_q for this purpose. To draw the crossover chiral and deconfinement transition lines, we define the dimensionless curvature matrix [104] as

$$\mathcal{C} = \begin{pmatrix} T^2 c_{\sigma_l\sigma_l} & T^2 c_{\sigma_l\sigma_s} & T^{-1} c_{\sigma_l\Phi} & T^{-1} c_{\sigma_l\bar{\Phi}} \\ T^2 c_{\sigma_s\sigma_l} & T^2 c_{\sigma_s\sigma_s} & T^{-1} c_{\sigma_s\Phi} & T^{-1} c_{\sigma_s\bar{\Phi}} \\ T^{-1} c_{\Phi\sigma_l} & T^{-1} c_{\Phi\sigma_s} & T^{-4} c_{\Phi\Phi} & T^{-4} c_{\Phi\bar{\Phi}} \\ T^{-1} c_{\bar{\Phi}\sigma_l} & T^{-1} c_{\bar{\Phi}\sigma_s} & T^{-4} c_{\bar{\Phi}\Phi} & T^{-4} c_{\bar{\Phi}\bar{\Phi}} \end{pmatrix}. \tag{3.24}$$

Here, we have used the notation

$$c_{xy} = \frac{\partial^2 \Omega_{\rm PNJL}}{\partial x \partial y}, \quad x, y = \{\sigma_l, \sigma_{\rm s}, \Phi, \bar{\Phi}\}. \tag{3.25}$$

The inverse of Eq. (3.24) yields the susceptibilities. We then determine the crossover transition point by the peak position of the corresponding susceptibilities.

Figure 3.3 presents the QCD phase diagram in the θ_l-T plane for the condition (I). In this case, the RW periodicity exists and hence we only plot the region $0 \leq \theta_l \leq \pi/3$. The dotted and the dot-dashed lines mean the crossover deconfinement transition line and the crossover chiral transition line, respectively. The vertical dashed line is the RW transition line at $\theta_l = \pi/3$. The remaining solid line stands for the first-order deconfinement transition line. Then, the three first-order lines merge at the RW end point, which means that the end point is a triple point. The RW end point can become a tricritical point, i.e., one first-order line and two second-order lines merge there. In Refs. [55, 103], it was found that the end point is tricritical if we choose

$$\mathcal{U}(\Phi, \bar{\Phi}) = -bT \left[54 \mathrm{e}^{-aT} \Phi\bar{\Phi} + \log H(\Phi, \bar{\Phi}) \right] \tag{3.26}$$

for the Polyakov-loop potential [98, 101], where a, b are the parameters and $H(\Phi, \bar{\Phi})$ is defined in Eq. (2.6). Furthermore, the 2+1-flavor EPNJL model also predicts the tricritical point [102]. More robust study may be needed to determine whether the end point is triple or tricritical point.

Now, let us move to the condition (II). We plot the QCD phase diagram in Fig. 3.4. The three dashed lines denote the first-order RW-like transition

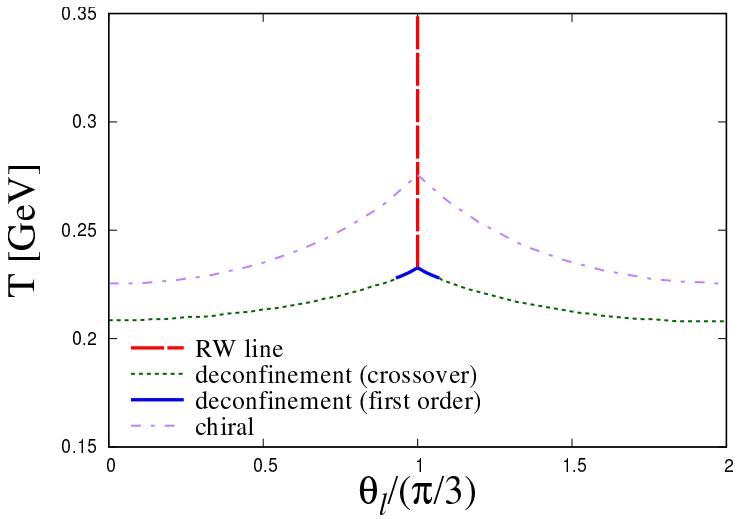

Figure 3.3: The QCD phase diagram for condition (I). The vertical dashed line is the first-order RW transition line. The dot-dashed line means the crossover chiral transition line, while dotted line does the crossover deconfinement transition line. The solid line denotes the first-order deconfinement transition line.

lines, while the meaning of the other lines is the same as in Fig 3.3. The symbols $\mathrm{E}_1, \mathrm{E}_2$, and E_3 are the locations of the RW-like end points; see Table 3.2. From the location of E_1, the RW-like transition starts at $\theta_l = 0.42\pi$, which is consistent with LQCD prediction $\theta_l \sim 0.45\pi$ in Ref. [39].

It is clearly seen that the RW periodicity disappears also for the phase diagram, and the analytic region is broader than that of the condition (I). The diagram is symmetric with respect to the line $\theta_l = \pi$. This property comes from the trivial periodicity of 2π in θ_l; see Appendix D. Due to this fact, the chiral and deconfinement transition lines are symmetric around E_2. On the contrary, the chiral transition line becomes discontinuous when it hits the RW-like transition line. As for the deconfinement transition line, the first-order region is asymmetric and it shrinks in comparison with the case of condition (I).

Next, we compare the chiral transition lines $T_{\mathrm{chiral}}(\theta_l)$ with LQCD calculations [40]. In Fig. 3.5, we present the ratio $R = T_{\mathrm{chiral}}(\theta_l)/T_{\mathrm{chiral}}(0)$ as a function of $(\theta_l/\pi)^2$ in which LQCD data are taken from Ref. [40]. The solid lines are the results of the model calculation. The PNJL model thus repro-

Table 3.2: The values of T and θ_l at the RW-like end point.

Point	E_1	E_2	E_3
$(T$ [MeV]$, \theta_l)$	$(236, 0.42\pi)$	$(246, \pi)$	$(236, 1.58\pi)$

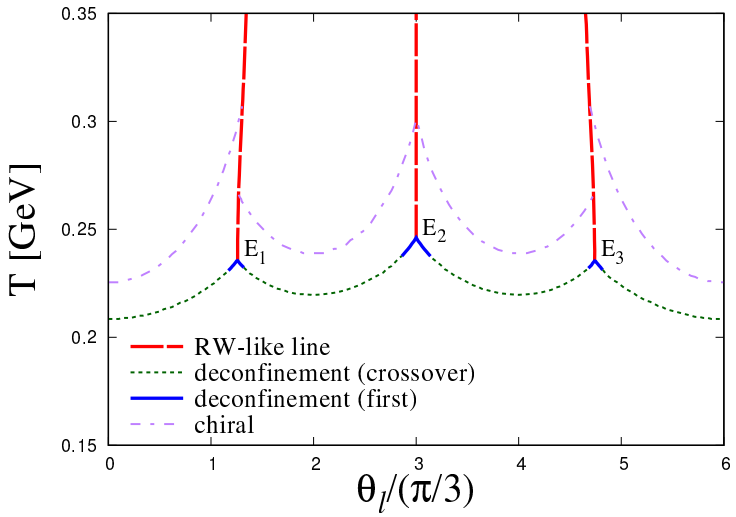

Figure 3.4: The QCD phase diagram for condition (II). The meaning of the lines is the same as in Fig. 3.4, except that the dashed line means the first-order RW-like transition line. The points E_1, E_2, E_3 correspond to the RW-like end point, respectively.

duces LQCD data considerably for condition (I) and is almost consistent for the condition (II).

Finally, let us concentrate on the region $0 \leq \theta_l \leq 2\pi/3$ and discuss the behavior of the RW-like transition line. The RW-like transition line starts at the point E_1, i.e., $(T^{\mathrm{RW}'}, \theta_l^{\mathrm{RW}'}) = (236\ \mathrm{MeV}, 0.42\pi)$. In addition, the transition point is located at $\theta_l^{\mathrm{c}} \sim 0.483\pi$ in the high-T limit [39]. Hence, as going away from the point, the transition line approaches θ_l^{c}. The transition line is well fitted by the polynomial function

$$\theta_l = 0.42\pi + a_1\xi + a_2\xi^2, \quad \xi = \frac{T - T^{\mathrm{RW}'}}{T^{\mathrm{RW}'}}, \tag{3.27}$$

around E_1 with $a_1 = -0.023$ and $a_2 = 0.93$, and its curvature $\partial^2\theta_l/\partial T^2$ indeed positive.

3.6.3 Analyticity of number density

From the previous analyses, it was found that the analytic region is expanded when we break extended $\mathbb{Z}_3$ symmetry, as shown for the condition (II). It is thus expected that we can obtain a broader analytic region if extended $\mathbb{Z}_3$ symmetry is broken more strongly. In this section, we calculate the imaginary part of the u- and s-quark number densities, $\mathrm{Im}(n_{\mathrm{u}})$ and $\mathrm{Im}(n_{\mathrm{s}})$, under the situation that two of θ_f are fixed to constants. In the calculation of $\mathrm{Im}(n_{\mathrm{u}})$, we treat θ_{u} and θ_{d} independently, while take $\theta_{\mathrm{u}} = \theta_{\mathrm{d}} = \theta_l$ in the calculation of $\mathrm{Im}(n_{\mathrm{s}})$.

In Fig. 3.6, we plot the T and θ_{u} dependence of $\mathrm{Im}(n_{\mathrm{u}})$. The left panel is the result for the case of $(\theta_{\mathrm{d}}, \theta_{\mathrm{s}}) = (\pi/4, 0)$ and the right panel corresponds

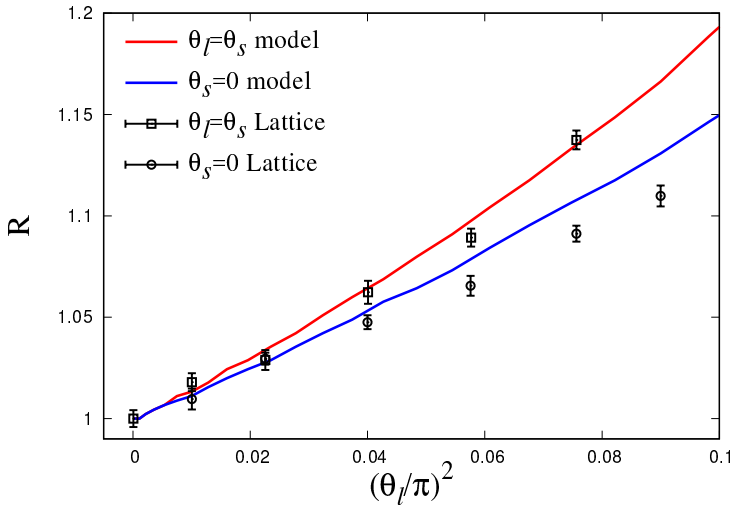

Figure 3.5: The chiral transition line for condition (I) and (II). The vertical axis is normalized by the transition temperature at $\theta_l = 0$. The solid lines are the model results, and the data with the error bars are LQCD results in Ref. [40].

to $(\theta_{\rm d}, \theta_{\rm s}) = (\pi/8, 0)$. The RW-like transition disappears in the right panel, and we then numerically checked that this situation is realized for $\theta_{\rm d} \leq \pi/8$ with $\theta_{\rm s} = 0$. Figure 3.7 presents $\mathrm{Im}(n_{\rm s})$ as a function of T and $\theta_{\rm s}$. In the left panel with $\theta_l = \pi/4$, the RW-like transition still occurs, but it is not seen for $\theta_l = \pi/5$. We also numerically confirmed that no RW-like transition takes place for $\theta_l \leq \pi/5$. These results indicate that the analytic continuation from $\theta_{\rm u}$ or $\theta_{\rm s}$ is more informative than the case that the RW periodicity exists, particularly for high T.

The extraction of s-quark number density at high T enables us to determine the strength $G_{\rm v,s}$ of the vector-type interaction acting only on the s-quark, $-G_{\rm v,s}(\bar{s}\gamma_\mu s)^2$. Under the MFA, this interaction shifts the s-quark chemical potential as $\tilde{\mu}_{\rm s} = \mu_{\rm s} - 2G_{\rm v,s}n_{\rm s}$, where $n_{\rm s}$ is the s-quark number density. Hence, $n_{\rm s}$ is sensitive to the value of $G_{\rm v,s}$ and inversely we can pin down the value of $G_{\rm v,s}$ from $n_{\rm s}$ calculated by LQCD simulations, like $G_{\rm v}$ in Chapter 2. The result in Fig. 3.7 suggests that the analytic continuation is good to calculate $n_{\rm s}$ at high T.

3.7 Short summary

In this chapter, we have studied properties of the QCD with finite $\mu_l = i\theta_l T$ and $\mu_{\rm s} = i\theta_{\rm s} T$. We first clarified the condition imposed on θ_l and $\theta_{\rm s}$ to realize the RW periodicity. The QCD exhibits the RW periodicity in general, but the RW periodicity is broken when θ_l and/or $\theta_{\rm s}$ is fixed to some constant value. The fact can be interpreted as whether the QCD partition function is

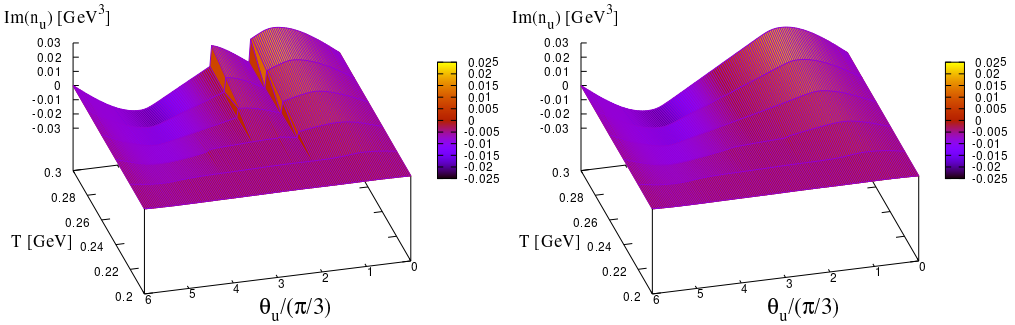

Figure 3.6: The T and $\theta_{\rm u}$ dependence of the imaginary part of the u-quark number density $n_{\rm u}$. The left panel is the result with $(\theta_{\rm d}, \theta_{\rm s}) = (\pi/4, 0)$, and the right panel corresponds to the one with $(\theta_{\rm d}, \theta_{\rm s}) = (\pi/8, 0)$.

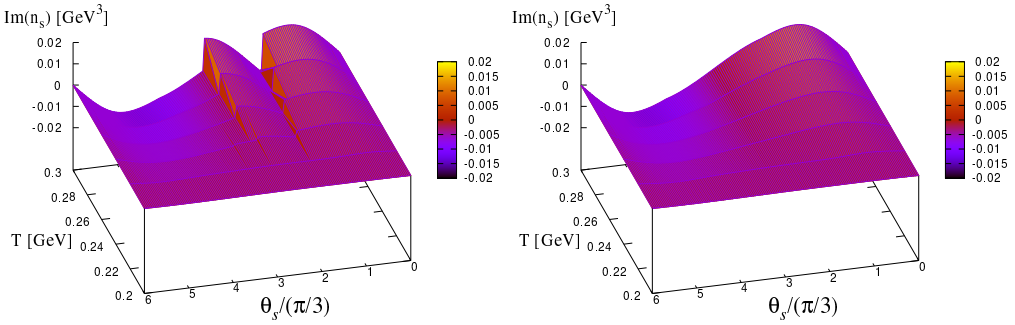

Figure 3.7: The T and $\theta_{\rm s}$ dependence of the imaginary part of the s-quark number density $n_{\rm s}$. The left panel is the result with $\theta_l = \pi/4$ and the right panel corresponds to the one with $\theta_l = \pi/5$.

invariant under the extended $\mathbb{Z}_3$ transformation or not. As a model with the same properties as the QCD at finite θ_l and $\theta_{\rm s}$, we introduced the 2+1-flavor PNJL model. Indeed, we showed that the thermodynamic potential of the PNJL model has extended $\mathbb{Z}_3$ symmetry unless any one of θ_l and $\theta_{\rm s}$ is taken to be some constant.

By using the PNJL model, we calculated the thermodynamic potential and the imaginary part of the quark number density, and drew the QCD phase diagram for the conditions (I) θ_l is varied with $\theta_{\rm s} = \theta_l$ and (II) θ_l is varied with $\theta_{\rm s} = 0$. The RW periodicity exists in all the results for condition (I). The behavior of the phase diagram is the same as in the 2-flavor case, i.e., the first-order RW transition takes place at $\theta_l = \pi/3$ and the quantities is a smooth function of θ_l at low T. As for condition (II), the RW periodicity is not seen, but the analytic region is broader than that of condition (I), as suggested in Ref. [39]. This property is advantageous for the analytic continuation from the imaginary chemical potential region to the real one.

The results obtained for condition (II) show that the analytic region is expanded by breaking the RW periodicity deliberately. Then, we considered

the situation that two imaginary chemical potentials are fixed, i.e., the RW periodicity is broken strongly. In such a situation, we calculated the imaginary part of the u-quark and s-quark number densities, $\mathrm{Im}(n_{\mathrm{u}})$ and $\mathrm{Im}(n_{\mathrm{s}})$. When $\theta_{\mathrm{s}} = 0$ and $\theta_{\mathrm{d}} \leq \pi/8$, $\mathrm{Im}(n_{\mathrm{u}})$ becomes smooth for any T and θ_{u}. For $\mathrm{Im}(n_{\mathrm{s}})$, analyticity is achived for any T and θ_{s} when $\theta_l \leq \pi/5$. If we perform LQCD calculation under these conditions, n_{u} and n_{s} at real chemical potential region can be extracted for $\mu_{\mathrm{u}}/T \gtrsim 1$ or $\mu_{\mathrm{s}}/T \gtrsim 1$; note that information is limited $\mu_{\mathrm{u}}/T \lesssim 1$ or $\mu_{\mathrm{s}} \lesssim 1$ for the case that the RW periodicity exists.

Chapter 4

QCD with isospin chemical potential

4.1 Introduction

In this section, we return to the 2-flavor QCD and take into account the isospin chemical potential $\mu_{\rm iso}$. In the inner core of neutron star, a highly isospin-asymmetric environment is realized, and hence we need to know properties of the QCD with finite $\mu_{\rm iso}$, in order to discuss whether the quark matter exists there. Based on the extracted knowledge, it is possible to improve the EPNJL model in Chapter 2 where the effects of $\mu_{\rm iso}$ are not included in the Lagrangian.

In both the real [42, 105, 106] and imaginary [55, 56, 57] $\mu_{\rm iso}$ regions, LQCD simulations become feasible because the fermion determinant has positivity, as shown later. Indeed, LQCD simulations were done so far, e.g., in Refs. [42, 43, 56, 57]. In the finite $\mu_{\rm iso}$ region, however, LQCD simulations become unfeasible due to the occurrence of the charged-pion condensate, i.e., the expectation value $\langle\pi^{\pm}\rangle$ does not vanish. The condensate starts at $\mu_{\rm iso} = m_\pi/2$ for zero temperature [44], while it occurs at $m_\pi/2 \leq \mu_{\rm iso}$ at finite T [107]. It was suggested in Refs. [53, 54, 73] that the average phase factor becomes almost zero in the condensed phase. The small value of the average factor means that the sign problem is severe, and LQCD simulations are thus hard to provide any results. Due to this, information on the quark matter under finite $\mu_{\rm iso}$ are limited. It is thus important to search the region where LQCD simulations with $\mu_{\rm iso}$ are easy to perform.

The candidate is the imaginary $\mu_{\rm iso} = i\theta_{\rm iso}T$ region. Here, $\theta_{\rm iso}$ is a dimensionless isospin chemical potential. In Ref. [57], it was demonstrated that the $\theta_{\rm iso}$ region is free from the sign problem. In addition, by employing the chiral perturbation theory and the PNJL model, Sakai *et al.* showed in Ref. [55] that that no pion condensate occurs there, at least, without the light-quark chemical potential μ_l. Our aim is to prove that the pion condensate does not take place, even including the imaginary $\mu_l = i\theta_l T$, by using

QCD inequalities.

In the following, we first explore the γ_5-hermiticity of the fermion determinant with real $\mu_{\rm iso}$ or imaginary $\mu_{\rm iso}$ in which imaginary μ_l is also considered. Positivity of the fermion determinant enables us to use QCD inequalities. We derive QCD inequalities and demonstrate that the charged-pion condensate does not occur for imaginary $\mu_{\rm iso}$ in the next section.

4.2 Fermion determinant and γ_5-hermiticity

Toward deriving QCD inequalities, we first discuss the γ_5-hermiticity of the fermion matrix in some cases. Our starting point is the two-flavor QCD Lagrangian with finite μ_l in Euclidean space-time:

$$\mathcal{L}_{\rm QCD} = \bar{q}(\gamma_\mu D_\mu + \hat{m} - \mu_l\gamma_4)q + \frac{1}{2g^2}{\rm Tr_c}F_{\mu\nu}F_{\mu\nu}, \tag{4.1}$$

where $q = ({\rm u}, {\rm d})^{\rm T}$ is the quark field and The current quark-mass matrix $\hat{m}$ is given by $\hat{m} = {\rm diag}(m_{\rm u}, m_{\rm d})$ with current u- and d-quark masses. The definition of the other symbols is the same as in Sec. 1.2.1. In the following discussion, we do not consider the θ term that breaks CP symmetry [1, 2, 3] since the term causes the sign problem [12, 102].

From Eq. (4.1), the QCD action and the QCD grand-canonical partition function are defined as

$$S_{\rm QCD} = \int_0^\beta d\tau \int d^3\boldsymbol{x}\mathcal{L}_{\rm QCD}, \tag{4.2}$$

$$Z_{\rm QCD} = \int \mathcal{D}A\mathcal{D}\bar{q}\mathcal{D}q \exp\left[-S_{\rm QCD}\right], \tag{4.3}$$

where $\beta = 1/T$. In Eq. (4.3), the quark field has a bilinear form and can be integrated out:

$$Z_{\rm QCD} = \int \mathcal{D}A{\rm Det}\mathcal{M}(\mu_l){\rm e}^{-S_{\rm G}} \equiv \int \mathcal{D}\mu(A), \tag{4.4}$$

$$\mathcal{D}\mu(A) = \mathcal{D}A{\rm Det}\mathcal{M}(\mu_l){\rm e}^{-S_{\rm G}}, \tag{4.5}$$

where $S_{\rm G}$ is the pure gauge action and $\mathcal{M}(\mu_l)$ is the two-flavor fermion matrix defined by

$$\mathcal{M}(\mu_l) = \gamma_\mu D_\mu + \hat{m} - \mu_l\gamma_4. \tag{4.6}$$

The symbol "Det" in Eq. (4.5) stands for the determinant for flavor, Dirac, and color indices. For $\mu_l = 0$ and $\mu_l = i\theta_l T$, positivity of the fermion determinant is guaranteed; see Eqs. (1.33) and (1.36). We then keep imaginary μ_l finite.

Now, we consider the finite isospin chemical potential, i.e., $\mu_{\rm iso} > 0$ or $\mu_{\rm iso} < 0$. In this case, u- and d-quarks do not degenerate and the corresponding chemical potentials $\mu_{\rm u}$ and $\mu_{\rm d}$ yield the relation

$$\mu_l = \frac{\mu_{\rm u} + \mu_{\rm d}}{2}, \quad \mu_{\rm iso} = \frac{\mu_{\rm u} - \mu_{\rm d}}{2}. \tag{4.7}$$

Inversely, $\mu_{\rm u}$ and $\mu_{\rm d}$ are represented by

$$\mu_{\rm u} = \mu_l + \mu_{\rm iso}, \quad \mu_{\rm d} = \mu_l - \mu_{\rm iso}, \tag{4.8}$$

respectively. For finite $\mu_{\rm iso}$, the QCD Lagrangian is changed into

$$\tilde{\mathcal{L}}_{\rm QCD} = \mathcal{L}_{\rm QCD} - \mu_{\rm iso}\bar{q}\gamma_4\tau^3 q \tag{4.9}$$

and isospin SU(2) symmetry is explicitly broken to $\mathrm{U(1)_{I_3}}$, where $\mathrm{I_3} = \tau^3/2$ for the third component τ^3 of the Pauli matrix. The fermion determinant thus becomes

$$\tilde{\mathcal{M}}(\mu_l, \mu_{\rm iso}) = \gamma_\mu D_\mu + \hat{m} - \mu_l\gamma_4 - \mu_{\rm iso}\gamma_4\tau^3. \tag{4.10}$$

4.2.1 γ_5-hermiticity for real $\mu_{\rm iso}$

We first consider the case that $\mu_{\rm iso}$ is real. Under the setting of $m_{\rm u} = m_{\rm d} = m_l$, Eq. (4.10) satisfies the relation

$$\tau^a\gamma_5\tilde{\mathcal{M}}(i\theta_l T, \mu_{\rm iso})\gamma_5\tau^a = \tilde{\mathcal{M}}^\dagger(i\theta_l T, \mu_{\rm iso}) \quad (a = 1, 2), \tag{4.11}$$

where τ^a means the first or the second component of the Pauli matrix. Here, the summation is not taken over a. From Eq. (4.11), it can be proved that the fermion determinant $\mathrm{Det}\tilde{\mathcal{M}}(i\theta_l T, \mu_{\rm iso})$ possesses positivity [109], because

$$\begin{aligned}
&\left\{\mathrm{Det}\tilde{\mathcal{M}}(i\theta_l T, \mu_{\rm iso})\right\}^* \\
&\quad = \left\{\mathrm{det}\mathcal{M}'(i\theta_l T + \mu_{\rm iso})\mathrm{det}\mathcal{M}'(i\theta_l T - \mu_{\rm iso})\right\}^* \\
&\quad = \mathrm{det}\mathcal{M}'(i\theta_l T - \mu_{\rm iso})\mathrm{det}\mathcal{M}'(i\theta_l T + \mu_{\rm iso}) \\
&\quad = \left|\mathrm{det}\mathcal{M}'(i\theta_l T + \mu_{\rm iso})\right|^2 \\
&\quad = \mathrm{Det}\tilde{\mathcal{M}}(i\theta_l T, \mu_{\rm iso}) \geq 0,
\end{aligned} \tag{4.12}$$

where

$$\mathcal{M}'(i\theta_l T \pm \mu_{\rm iso}) = \gamma_\mu D_\mu + m_l - (i\theta_l T \pm \mu_{\rm iso})\gamma_4 \tag{4.13}$$

is the one-flavor fermion matrix with $i\theta_l T \pm \mu_{\rm iso}$. In Eq. (4.12), the symbol "det" means the determinant only for Dirac and color indices. Note that

$$\gamma_5\mathcal{M}'(i\theta_l T \pm \mu_{\rm iso})\gamma_5 = \mathcal{M}'(i\theta_l T \mp \mu_{\rm iso}) \tag{4.14}$$

Table 4.1: In this table, we present whether positivity exists or not for two cases. The word "not" means that positivity of the measure does not exist.

	non-zero real μ_l	imaginary μ_l
real $\mu_{\rm iso}$	not	has positivity for $m_{\rm u} = m_{\rm d}$
imaginary $\mu_{\rm iso}$	not	has positivity for any $m_{\rm u}$ and $m_{\rm d}$

and hence

$$\{\det\mathcal{M}'(i\theta_l T \pm \mu_{\rm iso})\}^* = \det\mathcal{M}'(i\theta_l T \mp \mu_{\rm iso}). \tag{4.15}$$

This relation means that the one-flavor fermion determinant itself does not have positivity. From the discussions mentioned in Eq. (4.12), the measure

$$\mathcal{D}\tilde{\mu}(A) = \mathcal{D}A\mathrm{Det}\tilde{\mathcal{M}}(i\theta_l T, \mu_{\rm iso})\mathrm{e}^{-S_{\rm G}} \tag{4.16}$$

maintains positivity. Along this line, we also call Eq. (4.11) the γ_5-hermiticity.

4.2.2 γ_5-hermiticity for imaginary $\mu_{\rm iso}$

Next, we show that the fermion determinant also keeps positivity for $\mu_{\rm iso} = i\theta_{\rm iso}T$ with the dimensionless isospin chemical potential $\theta_{\rm iso}$ [1)]. For $\mu_{\rm iso} = i\theta_{\rm iso}T$, the fermion matrix does not satisfy Eq. (4.11), but rather fulfills

$$\gamma_5\tilde{\mathcal{M}}(i\theta_l T, i\theta_{\rm iso}T)\gamma_5 = \tilde{\mathcal{M}}^\dagger(i\theta_l T, i\theta_{\rm iso}T). \tag{4.17}$$

Here, the Pauli matrix τ^a is not needed to prove Eq. (4.17).

From this, the determinant

$$\mathrm{Det}\tilde{\mathcal{M}}(i\theta_l T, i\theta_{\rm iso}T) = \det\mathcal{M}'(i\theta_{\rm u}T)\det\mathcal{M}'(i\theta_{\rm d}T) \tag{4.18}$$

have positivity, since the relation

$$\gamma_5\mathcal{M}'(i\theta_f T)\gamma_5 = (\mathcal{M}'(i\theta_f T))^\dagger \tag{4.19}$$

is satisfied for $f = \mathrm{u}, \mathrm{d}$ and this type of γ_5-hermiticity guarantees positivity of the fermion determinant [15]. Here, we have used Eq. (4.13) and introduced $\theta_{\rm u}, \theta_{\rm d}$ as

$$\theta_{\rm u} = \theta_l + \theta_{\rm iso}, \quad \theta_{\rm d} = \theta_l - \theta_{\rm iso}. \tag{4.20}$$

From the discussions mentioned above, we can apply QCD inequalities to the case of imaginary μ_l and real $\mu_{\rm iso}$, and also for the case of imaginary μ_l and imaginary $\mu_{\rm iso}$; see Table 4.1. In the next section, we formulate QCD inequalities.

[1)] In this case, we need not to impose the condition $m_{\rm u} = m_{\rm d}$ for the proof of positivity. However, we keep $m_{\rm u} = m_{\rm d}$ and do not discuss the case of $m_{\rm u} \neq m_{\rm d}$ in this thesis. See, e.g., Ref. [108] for the discussion of $m_{\rm u} \neq m_{\rm d}$.

4.3 QCD inequalities and charged-pion condensate

The Lagrangian (4.1) has flavor $\mathrm{U(1)_{I_3}}$ symmetry. Here, flavor $\mathrm{U(1)_{I_3}}$ symmetry means that the Lagrangian is invariant under the following transformation:

$$q \to \mathrm{e}^{i\phi_{\mathrm{v}}\tau^3} q, \tag{4.21}$$

where ϕ_{v} is a rotational angle. However, the charged-pion condensate $\langle\pi^{\pm}\rangle$ breaks the symmetry, because the quantity $\langle\pi^{\pm}\rangle$ is not invariant for $q \to \mathrm{e}^{i\phi_{\mathrm{V}}\tau^3} q$. Then, flavor $\mathrm{U(1)_{I_3}}$ symmetry is spontaneously broken and one Nambu-Goldstone boson appears; the Nambu-Goldstone boson is π^+ when the condensate of π^- is realized and vice versa. From this fact, we should prove that $\pi^{\pm}$ cannot be the Nambu-Goldstone boson accompanied with the spontaneous breaking of $\mathrm{U(1)_{I_3}}$ symmetry in the imaginary μ_{iso} region.

4.3.1 QCD inequalities for general meson

QCD inequalities provide a powerful framework to see which symmetry is spontaneously broken or not [12, 44, 49, 52]. Now, we derive QCD inequalities for the meson operator $J_a(x) = \bar{q}(x)\Gamma_a q(x)$, where Γ_a is a product of the γ-matrix and the Pauli matrix, which is taken so as to reproduce a quantum number of the meson considered. The subscript a denotes the label of meson. Hereafter, we impose the condition $m_{\mathrm{u}} = m_{\mathrm{d}} = m_l$.

The meson correlator is defined by

$$\langle J_a(x) J_a^{\dagger}(0)\rangle_{q,A} = \frac{1}{Z_{\mathrm{QCD}}} \int \mathcal{D}A\mathcal{D}\bar{q}\mathcal{D}q J_a(x) J_a^{\dagger}(0) \exp\left[-S_{\mathrm{QCD}}\right], \tag{4.22}$$

where $J_a^{\dagger}(x) = \bar{q}(x)\bar{\Gamma}_a q(x)$ for $\bar{\Gamma}_a = \gamma_4\Gamma_a\gamma_4$. The quark integral can be performed by using the Matthews-Salam formula

$$\begin{aligned}\int \mathcal{D}\bar{q}\mathcal{D}q\ \bar{q}_i q_j \bar{q}_k q_l\ \mathrm{e}^{-\bar{q}Wq} \\ = \mathrm{Det}W\left\{(W^{-1})_{ji}(W^{-1})_{lk} - (W^{-1}_{li})(W^{-1})_{jk}\right\},\end{aligned} \tag{4.23}$$

where W is any matrix with color, flavor, Dirac indices and the subscript i represents all the three indices. After applying Eq. (4.23) to Eq. (4.22), we obtain

$$\begin{aligned}\langle J_a(x) J_a^{\dagger}(0)\rangle_{q,A} &= -\left\langle \mathrm{Tr}\left[S(x,0)\Gamma_a S(0,x)\bar{\Gamma}_a\right]\right\rangle_A \\ &\quad + \left\langle \mathrm{Tr}\left[S(x,x)\Gamma_a\right]\right\rangle_A \left\langle \mathrm{Tr}\left[S(0,0)\bar{\Gamma}_a\right]\right\rangle_A \\ &= \left\langle \mathrm{Tr}\left[S(x,0) i\Gamma_a S(0,x) i\bar{\Gamma}_a\right]\right\rangle_A \\ &\quad + \left\langle \mathrm{Tr}\left[S(x,x)\Gamma_a\right]\right\rangle_A \left\langle \mathrm{Tr}\left[S(0,0)\bar{\Gamma}_a\right]\right\rangle_A,\end{aligned} \tag{4.24}$$

where

$$\langle \mathcal{O} \rangle_A = \frac{1}{Z_{\rm QCD}} \int \mathcal{D}A \mathcal{O} {\rm Det}\mathcal{M}. \tag{4.25}$$

The first term on the right side of Eq. (4.24) is a connected piece and the second term corresponds to a disconnected piece. The quark propagator $S(x,y)$ is defined by $\langle x| \mathcal{M}^{-1} |y\rangle$.

If there is an operator P that yields the relation

$$\mathcal{M}^\dagger = P\mathcal{M}P^{-1}, \tag{4.26}$$

then the propagator satisfies

$$S(0,x) = PS^\dagger(x,0)P^{-1}. \tag{4.27}$$

After inserting Eq. (4.27) into Eq. (4.24) and employing the Cauchy-Schwartz inequality

$${\rm Tr}\left[AB^\dagger\right] \leq \sqrt{{\rm Tr}\left[AA^\dagger\right]}\sqrt{{\rm Tr}\left[BB^\dagger\right]}, \tag{4.28}$$

the right side of Eq. (4.24) can be rewritten into

$$\begin{aligned}\langle J_a(x) J_a^\dagger(0)\rangle_{q,A} \leq & \langle {\rm Tr}\left[S(x,0)S^\dagger(x,0)\right]\rangle_A \\ & + \langle {\rm Tr}\left[S(x,x)\Gamma_a\right]\rangle_A \langle {\rm Tr}\left[S(0,0)\bar{\Gamma}_a\right]\rangle_A .\end{aligned} \tag{4.29}$$

This is QCD inequalities.

For the flavor non-singlet meson channel, a disconnected piece in Eq. (4.29) vanishes. We will show in the next section that this is true for the charged-pion channel. For such a case, we thus obtain

$$\langle J_a(x) J_a^\dagger(0)\rangle_{q,A} \leq \langle {\rm Tr}\left[S(x,0)S^\dagger(x,0)\right]\rangle_A . \tag{4.30}$$

The asymptotic behavior (as $|x| \to \infty$) of $\langle J_a(x) J_a^\dagger(0)\rangle_{q,A}$ is described by

$$\langle J_a(x) J_a^\dagger(0)\rangle_{q,A} \sim {\rm e}^{-m_a|x|}, \tag{4.31}$$

where m_a is a ground-state mass of each channel a. Hence, a candidate of Nambu-Goldstone boson is in channel such that Eq. (4.30) is saturated.

4.3.2 QCD inequalities for charged pion

Now, we consider the fermion matrix with imaginary μ_l and real $\mu_{\rm iso}$. In this case, the matrix satisfies Eq. (4.11) and the quark propagator has the relation

$$S(0,x) = \tau^a \gamma_5 S^\dagger(x,0) \gamma_5 \tau^a. \tag{4.32}$$

Eq. (4.24) can thus be transformed into

$$\begin{aligned}\langle J_a(x)J_a^\dagger(0)\rangle_{q,A} &= \langle \mathrm{Tr}\left[S(x,0)\Gamma_a\tau^a i\gamma_5 S^\dagger(x,0)i\gamma_5\tau^a\bar{\Gamma}_a\right]\rangle_A \\ &\quad + \langle \mathrm{Tr}\left[S(x,x)\Gamma_a\right]\rangle_A \langle \mathrm{Tr}\left[S(0,0)\bar{\Gamma}_a\right]\rangle_A \\ &\leq \langle \mathrm{Tr}\left[S(x,0)S^\dagger(x,0)\right]\rangle_A \\ &\quad + \langle \mathrm{Tr}\left[S(x,x)\Gamma_a\right]\rangle_A \langle \mathrm{Tr}\left[S(0,0)\bar{\Gamma}_a\right]\rangle_A . \end{aligned} \tag{4.33}$$

For imaginary μ_{iso}, the inequality differs from Eq. (4.33) since the fermion matrix $\tilde{\mathcal{M}}(i\theta_l T, i\theta_{\mathrm{iso}}T)$ satisfies Eq. (4.17), rather than Eq. (4.11). Then, the quark propagator satisfies the relation

$$S(0,x) = \gamma_5 S^\dagger(x,0)\gamma_5. \tag{4.34}$$

Adopting the same procedure, we can obtain

$$\begin{aligned}\langle J_a(x)J_a^\dagger(0)\rangle_{q,A} &= \langle \mathrm{Tr}\left[S(x,0)\Gamma_a i\gamma_5 S^\dagger(x,0)i\gamma_5\bar{\Gamma}_a\right]\rangle_A \\ &\quad + \langle \mathrm{Tr}\left[S(x,x)\Gamma_a\right]\rangle_A \langle \mathrm{Tr}\left[S(0,0)\bar{\Gamma}_a\right]\rangle_A \\ &\leq \langle \mathrm{Tr}\left[S(x,0)S^\dagger(x,0)\right]\rangle_A \\ &\quad + \langle \mathrm{Tr}\left[S(x,x)\Gamma_a\right]\rangle_A \langle \mathrm{Tr}\left[S(0,0)\bar{\Gamma}_a\right]\rangle_A \end{aligned} \tag{4.35}$$

in the case of imaginary μ_{iso}.

Let us take $\Gamma_{\pi^\pm} = i\gamma_5\tau^{\pi^\pm}$ and consider the correlator of charged pion. The contribution of the disconnected piece vanishes for both real and imaginary μ_{iso}, because

$$\begin{aligned}\langle \mathrm{Tr}\left[S(x,x)i\gamma_5\tau^a\right]\rangle_A &= \langle \mathrm{Tr}\left[S(x,x)i\gamma_5\tau^a(\tau^3)^2\right]\rangle_A \\ &= -\langle \mathrm{Tr}\left[S(x,x)i\gamma_5\tau^a\right]\rangle_A \end{aligned} \tag{4.36}$$

for π^a. Here, we have used $[S(x,x),\tau^3]=0$. Therefore, the inequality (4.33) is saturated for $\pi^\pm$. The charged-pion condensate can thus come out for real μ_{iso}. On the contrary, the inequality (4.35) is not saturated for $\pi^\pm$, and hence there is no charged-pion condensate for imaginary μ_{iso}. These statements suggest that the results in Refs. [44, 55] still hold even when imaginary μ_l is finite.

4.4 Short summary

In this chapter, we have derived QCD inequalities at real and imaginary isospin chemical potential region (μ_{iso}). In the derivation, we also considered the imaginary light-quark chemical potential (μ_l). We showed that positivity of the QCD partition function is ensured for each case, but the structure of the γ_5-hermiticity is different. As a result, the charged-pion channel can become a Nambu-Goldstone boson of the spontaneous $\mathrm{U}_{\mathrm{I}_3}(1)$ symmetry breaking at real μ_{iso}. The pion condensate can thus occur there. Meanwhile,

this is not true for the case of imaginary $\mu_{\rm iso}$, and thereby the charged-pion condensate does not occur. From these analyses, the results in Refs. [44, 55] are not changed in the presence of imaginary μ_l.

As already mentioned in Sec. 4.1, the charged-pion condensate makes LQCD simulations unfeasible. In the imaginary $\mu_{\rm iso}$ region, however, not only the sign problem but also the charged-pion condensate does not take place, and hence the region is suitable to perform LQCD simulations to extract information on isospin-asymmetric quark matter, which leads to understanding of the quark matter in the inner core of neutron star.

Chapter 5

Summary

In this thesis, we have studied the three imaginary chemical potential regions: (A) the imaginary μ_l region, (B) the imaginary μ_l and $\mu_{\rm s}$ region, (C) the imaginary μ_l and $\mu_{\rm iso}$ region.

In Chapter 2, we have considered region (A), and have drawn the hadron-quark phase transition line by using some two-phase models. In the two-phase models, we have taken the EPNJL model with the vector-type interaction for the quark phase and the relativistic mean field (RMF) theory for the hadron phase. In the hadron phase, the three parameter sets are taken, i.e., TM1 [90], NL3 [91], and MTEC [92]. For the EPNJL model, We determined the strength $G_{\rm v}$ of the vector-type interaction at $\mu_l = 0$ from LQCD data on the quark number density calculated in region (A). The obtained value is $G_{\rm v} = 0.36 G_{\rm s}$, where $G_{\rm s}$ is the scalar-type interaction.

As for the hadron phase, three parameter sets taken in the RMF theory yield almost the same equation of state (EoS) for $\rho_{\rm B} \leq \rho_0$. On the contrary, the behavior of the EoS in the large $\rho_{\rm B}$ region is quite different among them. We then calculated the MR relation of neutron star with the three parameter sets and compared the model results with the observational data and the statistically estimated one. Eventually, we found that MTEC and TM1 are suitable. We then reconstructed four two-phase models (TPMa1, TPMa2, TPMb1, TPMb2) by using MTEC and TM1; see Table 2.5 for the definition. Among these models, TPMa1 and TPMb1 predict that the quark phase appears in the inner core of neutron star, while the quark phase is not realized for the other models. The hadron-quark phase transition line is found to be shifted toward large $\mu_{\rm B}$ direction by the presence of $G_{\rm v}$.

Next, we considered the density-dependent vector-type interaction $G_{\rm v}(n_l)$ by assuming a Gaussian form with a parameter b. The models TPMa3 and TPMb3 with $G_{\rm v}(n_l)$ are defined in Table 2.6. Assuming that the quark phase exists in the inner core of neutron star, we showed that the lower value of b is 0.001 for TPMa3 and TPMb3. Using the hadron-quark phase transition line with TPMa1 and TPMa3, we found that the critical baryon chemical potential $\mu_{\rm B}^{\rm c}$ at $T = 0$ lies in the region 1750 MeV $\leq \mu_{\rm B}^{\rm c} \leq$ 1910 MeV, if the

quark phase appears in the inner core of neutron star. As for TPMb1 and TPMb3, the corresponding is 1560 MeV $\leq \mu_{\rm B}^{\rm c} \leq$ 1860 MeV. These suggest that the upper value of $\mu_{\rm B}^{\rm c}$ hardly depends on the RMF theory taken.

In Chapter 3, we have studied properties of the QCD in region (B) where $\mu_l = i\theta_l T$ and $\mu_{\rm s} = i\theta_{\rm s} T$. We first clarified the condition to realize the RW periodicity. The QCD exhibits the RW periodicity in general, but the RW periodicity is broken when θ_l and/or $\theta_{\rm s}$ is fixed to some constant value. The fact is closely related to whether the QCD partition function is invariant under the extended $\mathbb{Z}_3$ transformation or not. As a model with the same properties as the QCD at finite θ_l and $\theta_{\rm s}$, we introduced the 2+1-flavor PNJL model. Indeed, we showed that the thermodynamic potential of the PNJL model has extended $\mathbb{Z}_3$ symmetry unless any one of θ_l and $\theta_{\rm s}$ is taken to be some constant.

Taking the PNJL model, we calculated the thermodynamic potential and the imaginary part of the quark number density, and drew the QCD phase diagram for two conditions: (I) θ_l is varied with $\theta_{\rm s} = \theta_l$ and (II) θ_l is varied with $\theta_{\rm s} = 0$. The RW periodicity exists in all quantities for condition (I). The behavior of the phase diagram is the same as in the 2-flavor case. Namely, the first-order RW transition takes place in $\theta_l = \pi/3$ and higher T, whereas the quantities are a smooth function of θ_l at lower T. As for condition (II), the RW periodicity is not seen. This means that the analytic region is broader than the case of condition (I), as suggested in Ref. [39]. This property is quite useful for the analytic continuation from the imaginary to the real chemical potential region.

The results obtained for condition (II) show that the analytic region is expanded by breaking the RW periodicity deliberately. Then, we considered the situation that two imaginary chemical potentials are fixed, i.e., the RW periodicity is broken strongly. For this situation, we calculated the imaginary part of the u-quark and s-quark number densities, ${\rm Im}(n_{\rm u})$ and ${\rm Im}(n_{\rm s})$. When $\theta_{\rm s} = 0$ and $\theta_{\rm d} \leq \pi/8$, ${\rm Im}(n_{\rm u})$ becomes smooth for any T and $\theta_{\rm u}$. Analyticity of ${\rm Im}(n_{\rm s})$ is realized for any T and $\theta_{\rm s}$, when $\theta_l \leq \pi/5$. If we make LQCD simulations under the conditions, $n_{\rm u}$ ($n_{\rm s}$) can be obtained for $\mu_{\rm u}/T \gtrsim 1$ ($\mu_{\rm s}/T \gtrsim 1$); note that information is limited in $\mu_{\rm u}/T \lesssim 1$ or $\mu_{\rm s}/T \lesssim 1$ for the case that the RW periodicity exists.

In Chapter 4, we investigated region (C). For this purpose, we aim at deriving QCD inequalities at real and imaginary isospin chemical potentials ($\mu_{\rm iso}$). In the derivation, we also considered the imaginary light-quark chemical potential (μ_l). We showed that positivity of the QCD partition function is ensured for each case, but the structure of the γ_5-hermiticity is different. As a result, the charged-pion channel can become a Nambu-Goldstone boson of the spontaneous ${\rm U_{I_3}}(1)$ symmetry breaking for real $\mu_{\rm iso}$. The pion condensate can thus occur there. Meanwhile, this is not the case for imaginary $\mu_{\rm iso}$, and thereby the charged-pion condensate does not occur. From these

analyses, we found that the results of Refs. [44, 55] are not changed even in the presence of imaginary $\mu_{\rm iso}$. The charged-pion condensate makes LQCD simulations unfeasible. In the imaginary $\mu_{\rm iso}$ region, however, not only the sign problem but also the charged-pion condensate does not take place, and hence the region is suitable to perform LQCD simulations to extract information on isospin-asymmetric quark matter at real $\mu_{\rm iso}$. This information is quite helpful for understanding of the quark matter in the inner core of neutron star.

Appendix

A Notations in Euclidean space-time

We summarize the notations used in Euclidean space-time. We move to Euclidean space-time by introducing new coordinates as

$$x_4^{\mathrm{E}} = \tau = ix^0, \quad x_i^{\mathrm{E}} = -x^i. \tag{A.1}$$

If we define Euclidean γ-matrices as

$$\gamma_4^{\mathrm{E}} = \gamma^0, \quad \gamma_i^{\mathrm{E}} = i\gamma^i, \tag{A.2}$$

then the operator $\gamma^\mu D_\mu$ is converted into $i\gamma_\mu^{\mathrm{E}} D_\mu^{\mathrm{E}}$, where the covariant derivative is $D_\mu^{\mathrm{E}} = \partial_\mu^{\mathrm{E}} + iA_\mu^{\mathrm{E}}$ with the Euclidean gauge field,

$$A_4^{\mathrm{E}} = -iA^0, \quad A_i^{\mathrm{E}} = A^i. \tag{A.3}$$

The Euclidean field strength $F_{\mu\nu}^{\mathrm{E}}$ is obtained from the relation:

$$F_{\mu\nu}^{\mathrm{E}} = \frac{1}{i}\left[D_\mu^{\mathrm{E}}, D_\nu^{\mathrm{E}}\right]. \tag{A.4}$$

As for the Euclidean γ-matrices, it should be noted that all the matrices γ_μ^{E} are hermitian. Finally, the matrix γ_5 is defined by

$$\gamma_5^{\mathrm{E}} = \gamma_1^{\mathrm{E}}\gamma_2^{\mathrm{E}}\gamma_3^{\mathrm{E}}\gamma_4^{\mathrm{E}}, \tag{A.5}$$

which returns to the Minkowski one $\gamma^5 = i\gamma^0\gamma^1\gamma^2\gamma^3$.

Under these preparations, Eq. (1.2) is transformed into

$$\mathcal{L}_{\mathrm{QCD}} \ \rightarrow \ -\mathcal{L}_{\mathrm{QCD}}^{\mathrm{E}} = -\left[\bar{q}(\gamma_\mu^{\mathrm{E}} D_\mu^{\mathrm{E}} + \hat{m})q + \frac{1}{2g^2}\mathrm{Tr_c} F_{\mu\nu}^{\mathrm{E}} F_{\mu\nu}^{\mathrm{E}}\right]. \tag{A.6}$$

Here, we define the Euclidean QCD Lagrangian $\mathcal{L}_{\mathrm{QCD}}^{\mathrm{E}}$, not including minus sign.

B Chiral transformation

In this section, we discuss $\mathrm{U}(2)_{\mathrm{R}} \otimes \mathrm{U}(2)_{\mathrm{L}}$ transformation. The unitary group $\mathrm{U}(N)$ can be represented as the direct product $\mathrm{U}(1) \otimes \mathrm{SU}(N)$, and hence

$$\mathrm{U}(2)_{\mathrm{R}} \otimes \mathrm{U}(2)_{\mathrm{L}} \simeq \mathrm{U}(1)_{\mathrm{R}} \otimes \mathrm{U}(1)_{\mathrm{R}} \otimes \mathrm{SU}(2)_{\mathrm{R}} \otimes \mathrm{SU}(2)_{\mathrm{L}}. \tag{B.7}$$

Furthermore, the right side of Eq. (B.7) can be rewritten as vector- and axial-types of transformations:

$$\begin{aligned}\mathrm{U(1)_R} \otimes \mathrm{U(1)_L} \otimes \mathrm{SU(2)_R} \otimes \mathrm{SU(2)_L} \\ \simeq \mathrm{U(1)_V} \otimes \mathrm{U(1)_A} \otimes \mathrm{SU(2)_V} \otimes \mathrm{SU(2)_A}.\end{aligned} \tag{B.8}$$

The transformation parameters on the right side of Eq. (B.8) is given by the linear combination of $\theta^a_{\mathrm{R,L}}$. We thus obtain four subgroups:

1. $\mathrm{U(1)_V}$ transformation

   This is a simple phase transformation defined by

   $$q \ \rightarrow \ \mathrm{e}^{i\alpha} q, \ \ \bar{q} \ \rightarrow \ \bar{q}\mathrm{e}^{-i\alpha}. \tag{B.9}$$

   The corresponding Noether current is given by $J_\mu = \bar{q}\gamma_\mu q$, and the conserved charge is the quark number.

2. $\mathrm{U(1)_A}$ transformation

   This transformation is the axial-type phase transformation:

   $$q \ \rightarrow \ \mathrm{e}^{i\gamma^5\beta} q, \ \ \bar{q} \ \rightarrow \ \bar{q}\mathrm{e}^{i\gamma^5\beta}. \tag{B.10}$$

   The Lagrangian (1.20) is invariant under the $\mathrm{U_A(1)}$ transformation if we persist in classical theory, and the Noether current is obtained as $J^5_\mu = \bar{q}\gamma_\mu\gamma^5 q$. Once we move to quantum theory, the symmetry is *explicitly* broken by quantum anomaly [1)]. This is well-known $\mathrm{U_A(1)}$ *anomaly* or *chiral anomaly* [9, 10].

3. $\mathrm{SU(2)_V}$ transformation

   $\mathrm{SU(2)_V}$ transformation is called the isospin transformation. The definition is

   $$q \ \rightarrow \ \mathrm{e}^{i\vec{\theta}\cdot\vec{\tau}} q, \ \ \bar{q} \ \rightarrow \ \bar{q}\mathrm{e}^{-i\vec{\theta}\cdot\vec{\tau}}, \tag{B.13}$$

   and corresponds to the rotation in 2-flavor space. The Noether current is given by $J^a_\mu = \bar{q}\gamma_\mu\tau^a q$.

4. $\mathrm{SU(2)_A}$ transformation

   This is *chiral transformation*. The chiral transformation is defined by

   $$q \ \rightarrow \ \mathrm{e}^{i\gamma^5\vec{\phi}\cdot\vec{\tau}} q, \ \ \bar{q} \ \rightarrow \ \bar{q}\mathrm{e}^{i\gamma^5\vec{\phi}\cdot\vec{\tau}}. \tag{B.14}$$

   The Noether current is $J^{a,5}_\mu = \bar{q}\gamma_\mu\gamma^5\tau^a q$. As an important point, the symmetry is *spontaneously* broken in the low-energy region, even if the Lagrangian preserves chiral symmetry at the beginning.

[1)] In the chiral limit, the divergence of $J_{\mu,5}$ becomes

$$\partial^\mu J^5_\mu = -\frac{2N_f}{16\pi^2}\mathrm{Tr_c}\left[F_{\mu\nu}\tilde{F}_{\mu\nu}\right], \tag{B.11}$$

$$\tilde{F}_{\mu\nu} = \frac{1}{2}\epsilon_{\mu\nu\rho\sigma}F_{\rho\sigma}, \tag{B.12}$$

with the number N_f of flavors.

C Mean field approximation to the 2+1-flavor PNJL model

We perform the mean-field approximation (MFA) to the scalar-type interaction and the KMT interaction in the 2+1-flavor PNJL model. First, we focus on the scalar-type interaction defined by

$$-G_{\rm s}\sum_{a=0}^{8}\left[(\bar{q}\lambda^a q)^2+(\bar{q}i\gamma^5\lambda^a q)^2\right]. \tag{C.15}$$

Hereafter, we omit the pseudo-scalar interaction, since we are interested only in the case that the vacuum preserves parity symmetry.

The remaining term has the flavor structure as

$$\sum_{a=0}^{8}(\bar{q}\lambda^a q)^2=\sum_{a=0}^{8}\bar{q}_f(\lambda^a)_{ff'}q_{f'}\bar{q}_g(\lambda^a)_{gg'}q_{g'}. \tag{C.16}$$

Here, flavor indices are denoted by f, f', g, g'. Equation (C.16) can be decomposed into

$$\bar{q}_f(\lambda^0)_{ff'}q_{f'}\bar{q}_g(\lambda^0)_{gg'}q_{g'}+\sum_{b=1}^{8}\bar{q}_f(\lambda^b)_{ff'}q_{f'}\bar{q}_g(\lambda^b)_{gg'}q_{g'}, \tag{C.17}$$

where $\lambda^0=\sqrt{2/3}\mathbf{1}_f$ for the unit matrix $\mathbf{1}_f$ in flavor space. After using the complete relation of the Gell-Mann matrices,

$$\sum_{b=1}^{8}(\lambda^b)_{ff'}(\lambda^b)_{gg'}=2\left[\delta_{f'g}\delta_{fg'}-\frac{1}{3}\delta_{ff'}\delta_{gg'}\right], \tag{C.18}$$

we reach the expression

$$\sum_{a=0}^{8}(\bar{q}\lambda^a q)^2=2\bar{q}_f q_g\bar{q}_g q_f. \tag{C.19}$$

If we do not consider the Fock term, we can apply the replacement

$$\bar{q}_f q_g\bar{q}_g q_f\to\langle\bar{q}_f q_g\rangle\,\bar{q}_g q_f+\langle\bar{q}_g q_f\rangle\,\bar{q}_f q_g-\langle\bar{q}_f q_g\rangle\,\langle\bar{q}_g q_f\rangle \tag{C.20}$$

for Eq. (C.19) [60]. Furthermore, by assuming $\langle\bar{q}_f q_{f'}\rangle=0$ for $f\neq f'$, the scalar-type interaction under the mean-field approximation is given by

$$-G_{\rm s}\sum_{a=0}^{8}\left[(\bar{q}\lambda^a q)^2+(\bar{q}i\gamma^5\lambda^a q)^2\right]\to-4G_{\rm s}\sum_f\sigma_f\bar{q}_f q_f+2G_{\rm s}\sum_f\sigma_f^2, \tag{C.21}$$

where $\sigma_f=\langle\bar{q}_f q_f\rangle$, i.e., the chiral condensate for each flavor.

Next, we consider the KMT interaction,

$$K\left[\det{}_{f,f'}\bar{q}(1+\gamma_5)q+\det{}_{f,f'}\bar{q}(1-\gamma_5)q\right]. \tag{C.22}$$

The explicit form of the determinant is

$$\det \begin{pmatrix} \bar{\mathrm{u}}\Gamma^{\pm}\mathrm{u} & \bar{\mathrm{u}}\Gamma^{\pm}\mathrm{d} & \bar{\mathrm{u}}\Gamma^{\pm}\mathrm{s} \\ \bar{\mathrm{d}}\Gamma^{\pm}\mathrm{u} & \bar{\mathrm{d}}\Gamma^{\pm}\mathrm{d} & \bar{\mathrm{d}}\Gamma^{\pm}\mathrm{s} \\ \bar{\mathrm{s}}\Gamma^{\pm}\mathrm{u} & \bar{\mathrm{s}}\Gamma^{\pm}\mathrm{d} & \bar{\mathrm{s}}\Gamma^{\pm}\mathrm{s} \end{pmatrix} \tag{C.23}$$

for $\Gamma^{\pm} = 1 \pm \gamma_5$. Dropping the term including γ_5 and repeating the assumption of $\langle \bar{q}_f q_{f'} \rangle = 0$ for $f \neq f'$, we get

$$\det \begin{pmatrix} \bar{\mathrm{u}}\mathrm{u} & 0 & 0 \\ 0 & \bar{\mathrm{d}}\mathrm{d} & 0 \\ 0 & 0 & \bar{\mathrm{s}}\mathrm{s} \end{pmatrix} = (\bar{\mathrm{u}}\mathrm{u})(\bar{\mathrm{d}}\mathrm{d})(\bar{\mathrm{s}}\mathrm{s}). \tag{C.24}$$

For Eq. (C.24), the replacement

$$\bar{q}_f q_f \bar{q}_g q_g \bar{q}_h q_h \to \sum_{f,g,h:\mathrm{cyclic}} \langle \bar{q}_f q_f \rangle \langle \bar{q}_g q_g \rangle \bar{q}_h q_h - 2 \langle \bar{q}_f q_f \rangle \langle \bar{q}_g q_g \rangle \langle \bar{q}_h q_h \rangle \tag{C.25}$$

is available when neglecting the Fock term [60]. In Eq. (C.25), the summation is taken cyclicly for the flavor indices f, g, h. After applying Eq. (C.25) to Eq. (C.24), we can obtain

$$\begin{aligned} & K\Big[\det{}_{f,f'} \bar{q}(1+\gamma_5)q + \det{}_{f,f'} \bar{q}(1-\gamma_5)q\Big] \\ & \quad \to 2K\sigma_{\mathrm{d}}\sigma_{\mathrm{s}}\bar{\mathrm{u}}\mathrm{u} + 2K\sigma_{\mathrm{s}}\sigma_{\mathrm{u}}\bar{\mathrm{d}}\mathrm{d} + 2K\sigma_{\mathrm{d}}\sigma_{\mathrm{u}}\bar{\mathrm{s}}\mathrm{s} - 4K\sigma_{\mathrm{u}}\sigma_{\mathrm{d}}\sigma_{\mathrm{s}}. \end{aligned} \tag{C.26}$$

D Some properties of physical quantity at finite θ_l

We summarize some properties for some physical quantity $\mathcal{O}(\theta_l)$ as a function of θ_l. We denote $\mathcal{O}_{\mathrm{even}}(\theta_l)$ if $\mathcal{O}(\theta_l)$ is charge-even, while $\mathcal{O}_{\mathrm{odd}}(\theta_l)$ for charge-odd. In the following, the quantity ϵ stands for an infinitesimal real and positive number.

1. By definition,

$$\mathcal{O}_{\mathrm{even}}(\theta_l - \epsilon) = \mathcal{O}_{\mathrm{even}}(-\theta_l + \epsilon) \tag{D.27}$$

are satisfied. The QCD has a trivial periodicity of 2π in θ_l, since the boundary condition of the quark field is invariant under $\theta_l \to \theta_l + 2\pi$. We thus obtain

$$\mathcal{O}_{\mathrm{even}}(\theta_l - \epsilon) = \mathcal{O}_{\mathrm{even}}(-\theta_l + 2\pi + \epsilon). \tag{D.28}$$

Substituting $\theta_l = \pi$, it is found that charge-even quantities, such as the chiral and deconfinement transition lines, are symmetric with respect to the line $\theta_l = \pi$.

2. For charge-even quantity with the RW periodicity, the relation

$$\begin{aligned}\mathcal{O}_{\rm even}(\theta_l-\epsilon) &= \mathcal{O}_{\rm even}(-\theta_l+\epsilon)\\ &= \mathcal{O}_{\rm even}(-\theta_l+2\pi/3+\epsilon)\end{aligned} \tag{D.29}$$

is satisfied due to the RW periodicity. For $\theta_l=\pi/3$

$$\mathcal{O}_{\rm even}(\pi/3-\epsilon)=\mathcal{O}_{\rm even}(\pi/3+\epsilon), \tag{D.30}$$

and hence $\mathcal{O}_{\rm even}(\theta_l)$ is line-symmetrical with respect to the line of $\theta_l=\pi/3$. In the limit $\epsilon\to 0$, $\mathcal{O}_{\rm even}(\theta_l)$ can have a cusp if

$$\lim_{\epsilon\to+0}\frac{\mathcal{O}_{\rm even}(\theta_l\pm\epsilon)-\mathcal{O}_{\rm even}(\theta)}{\epsilon} \tag{D.31}$$

is neither zero nor infinity. This property is seen for the thermodynamic potential of the PNJL model in the high-T region; see Fig. 3.1.

3. For charge-odd quantity with the RW periodicity, the relation

$$\begin{aligned}\mathcal{O}_{\rm even}(\theta_l-\epsilon) &= -\mathcal{O}_{\rm even}(-\theta_l+\epsilon)\\ &= -\mathcal{O}_{\rm even}(-\theta_l+2\pi/3+\epsilon)\end{aligned} \tag{D.32}$$

is obtained, instead of Eq. (D.29). For $\theta_l=\pi/3$, we then obtain

$$\mathcal{O}_{\rm even}(\pi/3-\epsilon)=-\mathcal{O}_{\rm even}(\pi/3+\epsilon). \tag{D.33}$$

This means that charge-odd quantity can become discontinuous when $\epsilon\to+0$ and the quantity is finite in the limit. For example, the quark number density possesses a discontinuity on the line of $\theta_l=\pi/3$; see Fig. 3.1.

Bibliography

[1] A. A. Belavin, A. M. Polyakov, A. S. Schwartz, and Yu. S. Tyupkin, Phys. Lett. B **59**, 85 (1975).

[2] G. 't Hooft, Phys. Rev. Lett. **37**, 8 (1976).

[3] G. 't Hooft, Phys. Rev. D **14**, 3432 (1976); **18**, 2199(E) (1978).

[4] C. Patrignani *et al.* (Particle Data), Chin. Phys. C **40**, 100001 (2016).

[5] D. Gross and F. Wilczek, Phys. Rev. Lett. **30**, 1343 (1973).

[6] H. D. Politzer, Phys. Rev. Lett. **30**, 1346 (1973).

[7] M. Le Bellac, *Thermal Field Theory*, Cambridge Monographs on Mathematical Physics (2000).

[8] L. D. McLerran and B. Svetitsky, Phys. Rev. D **24**, 450 (1981).

[9] S. L. Adler, Phys. Rev. **177**, 2426 (1969).

[10] J. S. Bell and R. Jackiw, Nuovo Cim. **60A**, 47 (1969).

[11] Y. Nambu and J. Jona-Lasinio, Phys. Rev. **122**, 345 (1961); **124**, 246 (1961).

[12] C. Vafa and E. Witten, Nucl. Phys. B **234**, 173 (1984).

[13] J. Goldstone, Nuovo Cimento **19**, 154 (1961); J. Goldstone, A. Salam, and S. Weinberg, Phys. Rev. **127**, 965 (1962).

[14] H. Fukaya *et al.*, Phys. Rev. D **83**, 074501 (2011).

[15] M. Stephanov, arXiv:0701002.

[16] P. Bruan-Munzinger and J. Wambach, Rev. Mod. Phys. **81**, 1031 (2009).

[17] K. Fukushima and T. Hatsuda, Rept. Prog. Phys. **74**, 014001 (2011).

[18] K. Fukushima and C. Sasaki, Prog. Part. Nucl. Phys. **72**, 99 (2013).

[19] M. G. Alford, A. Schmitt, K. Rajagopal, and T. Schäfer, Rev. Mod. Phys. **80**, 1455 (2008).

[20] N. Cabibbo and G. Parisi, Phys. Lett. **B59**, 67 (1975).

[21] R. Hagedorn, Nuovo Cimento Suppl. **3**, 147 (1965); R. Hagedorn and J. Ranft, Nuovo Cimento Suppl. **6**, 169 (1968).

[22] F. Karsch, Lect. Notes Phys. **583**, 209 (2002).

[23] Y. Aoki, G. Endrodi, Z. Fodor, S. D. Katz, and K. K. Szabo, Nature **443**, 675 (2006); Y. Aoki, Z. Fodor, S. D. Katz, and k. K. Szabo, Phys. Lett. **B643**, 46 (2006).

[24] Z. Fodor and S. D. Katz, arXiv:0908.3341.

[25] M. Asakawa and K. Yazaki, Nucl. Phys. **A504**, 668 (1989).

[26] S. Borsanyi, EPJ Web Conf. **137**, 01006 (2017).

[27] Z. H. Li, U. Lombardo, H. -J. Schulze, W. Zuo, L. W. Chen, H. R. Ma, Phys. Rev. C **74**, 047304 (2006).

[28] M. Kohno, Phys. Rev. C **86**, 061301(R) (2012).

[29] Y. Yamamoto, T. Furumoto, N. Yasutake, and T. Rijken, Phys. Rev. C **90**, 045805 (2014); Eur. Phys. J. A **52**, 19 (2016); JPS Conf. Proc. **17**, 101003 (2017).

[30] H. -J. Schulze and T. Rijken, Phys. Rev. C **84**, 035801 (2011).

[31] H. Heiselberg and M. H. -Jensen, Phys. Rep. **328**, 237 (2000).

[32] P. B. Demorest, T. Pennucci, S. M. Ransom, M. S. E. Roberts, and J. W. T. Hassels, Nature **467**, 1081 (2010).

[33] J. Antoniadis *et al.*, Science **340**, 1233232 (2013).

[34] P. de Forcrand, *Proc. Sci.*, LAT2009 (2009) 010.

[35] K. Wilson, Phys. Rev. D **10**, 2445 (1974).

[36] P. de Forcrand and O. Philipsen, Nucl. Phys. **B642**, 290 (2002); **B673**, 170 (2003).

[37] M. D'Elia and M. P. Lambardo, Phys. Rev. D **67**, 014505 (2003); **70**, 074509 (2004).

[38] A. Roberge and N. Weiss, Nucl. Phys. **B275**, 734 (1986).

[39] C. Bonati, M. D'Elia, M. Mariti, M. Mesiti, F. Negro, and F. Sanfilippo, Phys. Rev. D **90**, 114025 (2014).

[40] C. Bonati, M. D'Elia, M. Mariti, M. Mesiti, F. Negro, and F. Sanfilippo, Phys. Rev. D **92**, 114025 (2015).

[41] C. Bonati, M. D'Elia, M. Mariti, M. Mesiti, F. Negro, and F. Sanfilippo, Phys. Rev. D **93**, 114025 (2016).

[42] J. B. Kogut and D. K. Sinclair, Phys. Rev. D **66**, 034505 (2002); **70**, 094501 (2004).

[43] W. Detmold, K. Orginos, and Z. Shi, Phys. Rev. D **86**, 054507 (2012).

[44] D. T. Son and M. A. Stephanov, Phys. Rev. Lett. **86**, 592 (2001).

[45] D. Weingarten, Phys. Rev. Lett. **51**, 1830 (1983).

[46] E. Witten, Phys. Rev. Lett. **51**, 2351 (1983).

[47] S. Nussinov, Phys. Rev. Lett. **52**, 966 (1984).

[48] D. Espriu, M. Gross, and J. F. Wheater, Phys. Lett. **B146**, 67 (1984).

[49] C. Vafa and E. Witten, Phys. Rev. Lett. **53**, 535 (1984).

[50] J. B. Kogut, M. A. Stephanov, and D. Toublan, Phys. Lett. **B464**, 183 (1999).

[51] J. B. Kogut, M. A. Stephanov, D. Toublan, J. J. M. Verbaarschot, and A. Zhitnitsky, Nucl. Phys. **B582**, 477 (2000).

[52] S. Nussinov and M. A. Lampert, Phys. Rept. **362**, 193 (2002).

[53] K. Splittorff, arXiv:hep-lat:0505001.

[54] J. Han and M. A. Stephanov, Phys. Rev. D **78**, 054507 (2008).

[55] Y. Sakai, H. Kouno, and M. Yahiro, J. Phys. G **37**, 105007 (2010).

[56] P. Cea, L. Cosmai, M. D'Elia, C. Manneschi, and A. Papa, Phys. Rev. D **80**, 034501 (2009); **81**, 094502 (2010); **85**, 094512 (2012).

[57] M. D'Elia and F. Sanfilippo, Phys. Rev. D **80**, 014502 (2009).

[58] Y. Sakai, T. Sasaki, H. Kouno, and M. Yahiro, Phys. Rev. D **82**, 076003 (2010).

[59] J. Takahashi, H. Kouno, and M. Yahiro, Phys. Rev. D **91**, 014501 (2015).

[60] T. Hatsuda and T. Kunihoro, Phys. Rept. **247**, 221 (1994).

[61] S. P. Klevanski, Rev. Mod. Phys. **64**, 649 (1992).

[62] M. Ishii, T. Sasaki, K. Kashiwa, H. Kouno, and M. Yahiro, Phys. Rev. D **89**, 071901 (2014).

[63] M. Ishii, K. Kashiwa, J. Takahashi, H. Kouno, and M. Yahiro, Phys.Rev. D **93**, 016002 (2016).

[64] M. Ishii, H. Kouno, and M. Yahiro, Phys. Rev D **95**, 114022 (2017).

[65] T. Sasaki, N. Yasutake, M. Kohno, H. Kouno, and M. Yahiro, arXiv:1307.0681.

[66] O. Lourenco, M. Dutra, A. Delfino, and M. Malheiro, Phys. Rev. D **84**, 125034 (2011).

[67] J. Sugano, J. Takahashi, M. Ishi, H. Kouno, and M. Yahiro, Phys. Rev. D **90**, 037901 (2014).

[68] S. Rößner, C. Ratti, and W. Weise, Phys. Rev. D **75**, 034007 (2007); C. Ratti, S. Rößner, M. A. Thaler, and W. Weise, Eur. Phys. J . C **49**, 213 (2007).

[69] M. Kaczmarek and F. Zantow, Phys. Rev. D **71**, 114510 (2005).

[70] B. -J. Schaefer, J. M. Pawlowski, and J. Wambach, Phys. Rev. D **76**, 074023 (2007).

[71] T. Sasaki, Y. Sakai, H. Kouno, and M. Yahiro, Phys. Rev. D **82**, 116004 (2010).

[72] H. Ueda, T. Z. Nakano, A. Ohnishi, M. Ruggieri, and K. Sumiyoshi, Phys. Rev. D **88**, 074006 (2013).

[73] Y. Sakai, T. Sasaki, H. Kouno, and M. Yahiro, Phys. Rev. D **82**, 096007 (2010).

[74] N. Bratovic, T. Hatsuda, and W. Weise, Nucl. Phys. **B719**, 131 (2013).

[75] S. Ejiri, Y. Maezawa, N. Ukita, S. Aoki, T. Hatsuda, N. Ishii, K. Kanaya, and T. Umeda (WHOT-QCD Collaboration), Phys. Rev. D **82**, 014508 (2010).

[76] K. Kashiwa, T. Hell, and W. Weise, Phys. Rev. D **84**, 056010 (2011).

[77] M. Baldo, I. Bombaci, and G. F. Burgio, Astron. Astrophys. **328**, 274 (1997).

[78] M. Kohno, Prog. Theor. Exp. Phys. **2015**, 123D02 (2015).

[79] R. Brockmann and R. Machleidt, Phys. Rev. C **42**, 1965 (1990).

[80] R. B. Wiringa, V. G. J. Stoks, and R. Schiavilla, Phys. Rev. C **51**, 38 (1995).

[81] A. Akmal, V. R. Pandharipande, and D. G. Ravenhall, Phys. Rev. C **58**, 1804 (1998).

[82] M. Takano, H. Togashi, and H. Kanzawa, Prog. Theor. Phys. Suppl. **186**, 63 (2010).

[83] H. Togashi, E. Hiyama, M. Takano, JPS Conf. Proc. **14**, 020812 (2017); **17**, 102002 (2017).

[84] J. D. Walecka, Ann. Phys. **83**, 491 (1974).

[85] B. D. Serot and J. D. Walecka, Adv. Nucl. Phys. **16**, 1 (1986).

[86] S. Borsanyi, G. Endrodi, Z. Fodor, A. Jakovac, S. D. Katz, S. Kreig, C. Ratti, K. K. Szabo, JHEP **1011**, 077 (2010).

[87] S. Borsanyi, Z. Fodor, S. D. Katz, S. Kreig, C. Ratti, K. Szabo, JHEP **1201**, 138 (2012).

[88] A. Bazavov *et al.* (HotQCD Collaboration), Phys. Rev. D **90**, 094503 (2014).

[89] M. Dutra, O. Lourenco, S. S. Avancini, B. V. Carlson, A. Delfino, J. Federal, D. P. Menezes, C. Providencia, S. Typel, and J. R. Stone, Phys. Rev. C **90**, 055203 (2014).

[90] K. Sumiyoshi, H. Kuwabara, and H. Toki, Nucl. Phys. **A581**, 725 (1995).

[91] G. A. Lalazissis, J. König, and P. Ring, Phys. Rev. C **55**, 540 (1997).

[92] T. Maruyama, T. Tatsumi, T. Endo, and S. Chiba, RecentRes. Devel. Phys. **7**, 1 (2006).

[93] A. W. Steiner, J. M. Lattimer, and E. F. Brown, Astrophys. J. **722**, 33 (2010).

[94] S. L. Shapiro and S. A. Teukolsky, *Black Holes, White Dwarfs, and Neutron Stars* (John Wiley & Sons, New York, 1983).

[95] K. Masuda, T. Hatsuda, and T. Takatsuka, Astrophys. J. **764**, 12 (2013); Prog. Theor. Exp. Phys. **2013**, 073D01 (2013).

[96] Y. Sakai, K. Kashiwa, H. Kouno, and M. Yahiro, Phys. Rev. D **77**, 051901(R) (2008); **78**, 036001 (2008).

[97] Y. Sakai, K. Kashiwa, H. Kouno, M. Matsuzaki, and M. Yahiro, Phys. Rev D **78**, 076007 (2008); **79**, 096001 (2009).

[98] K. Fukushima, Phys. Rev. D **77**, 114028 (2008); **78**, 114019 (2008).

[99] M. Kobayashi and T. Maskawa, Prog. Theor. Phys. **44**, 1422 (1970); M. Kobayashi, H. Kondo, and T. Maskawa, Prog. Theor. Phys. **45**, 1955 (1971).

[100] P. Rehberg, S. P. Klevanski, and J. Hüfner, Phys. Rev. C **53**, 410 (1996).

[101] K. Fukushima, Phys. Lett. **B591**, 277 (2004).

[102] T. Sasaki, H. Kouno, and M. Yahiro, Phys. Rev. D **87**, 056003 (2013).

[103] H. Kouno, Y. Sakai, K. Kashiwa, and M. Yahiro, J. Phys. G **39**, 035004 (2009).

[104] C. Sasaki, B. Friman, and K. Redlich, Phys. Rev. D **75**, 074013 (2007).

[105] M. Alford, A. Kapustin, and F. Wilczek, Phys. Rev. D **59**, 054502 (1999).

[106] K. Kashiwa and A. Ohnishi, Phys. Lett. **B772**, 669 (2017).

[107] B. B. Brandt, G. Endrődi, and S. Schmalzbauer, arXiv:1709.10487.

[108] M. Creutz, arXiv:hep-lat/0508012.

[109] H. Kouno, M. Kishikawa, T. Sasaki, Y. Sakai, and M. Yahiro, Phys. Rev. D **85**, 016001 (2012).